# Reconstruction of temperature, accumulation rate, and layer thinning from an ice core at South Pole, using a statistical inverse method

**Emma C. Kahle[1], Eric J. Steig[1], Tyler R. Jones[2], T.J. Fudge[1], Michelle R. Koutnik[1], Valerie A. Morris[2], Bruce H. Vaughn[2], Andrew J. Schauer[1], C. Max Stevens[1], Howard Conway[1], Edwin D. Waddington[1], Christo Buizert[3], Jenna Epifanio[3], James W. C. White[2]**

[1]Department of Earth and Space Sciences, University of Washington, Seattle WA 98195, USA
[2]Institute of Arctic and Alpine Research, University of Colorado, Boulder CO 80309, USA
[3]College of Earth Ocean and Atmospheric Sciences, Oregon State University, Corvallis OR 97331, USA

**Key Points:**

- An inverse method using a firn model with isotope diffusion provides self-consistent temperature, accumulation rate, and thinning histories.
- Glacial-interglacial temperature change at the South Pole was 6.7 +/- 1.0 K. The d18O/T sensitivity is 0.99 +/- 0.03 permille/K.
- Reconstruction of ice thinning shows millennial-scale variations in thinning function and decreased thinning at depth compared to 1-D model.

Corresponding author: Emma C. Kahle, eckahle@uw.edu

**Abstract**

Data from the South Pole ice core (SPC14) are used to constrain climate conditions and ice-flow-induced layer thinning for the last 54,000 years. Empirical constraints are obtained from the SPC14 ice and gas timescales, used to calculate annual-layer thickness and the gas-ice age difference ($\Delta$age), and from high-resolution measurements of water isotopes, used to calculate the water-isotope diffusion length. Both $\Delta$age and diffusion length depend on firn properties and therefore contain information about past temperature and snow-accumulation rate. A statistical inverse approach is used to obtain an ensemble of reconstructions of temperature, accumulation-rate, and thinning of annual layers in the ice sheet at the SPC14 site. The traditional water-isotope/temperature relationship is not used as a constraint; the results therefore provide an independent calibration of that relationship. The temperature reconstruction yields a glacial-interglacial temperature change of $6.7\pm1.0$°C at the South Pole. The sensitivity of $\delta^{18}0$ to temperature is $0.99\pm0.03$‰°C$^{-1}$, significantly greater than the spatial slope of 0.8‰°C$^{-1}$ that has been used previously to determine temperature changes from East Antarctic ice core records. The reconstructions of accumulation rate and ice thinning show millennial-scale variations in the thinning function as well as decreased thinning at depth compared to the results of a 1-D ice flow model, suggesting influence of bedrock topography on ice flow.


## 1 Introduction

Ice cores from polar ice sheets provide important records of past changes in climate and ice dynamics. Temperature and snow-accumulation rate are critical targets for reconstruction from ice-core data (Lorius et al., 1990). The traditional approach to reconstructing temperature is the use of water isotope ratios ($\delta^{18}$O, $\delta$D), calibrated using empirical relationships (Dansgaard, 1964; Jouzel et al., 1993). Another approach is borehole thermometry, which provides a direct measurement of the modern temperature profile of the ice sheet that can be related to surface temperature history through a heat advection-diffusion model (Cuffey et al., 1995; Dahl-Jensen et al., 1998). Finally, measurements of $\delta^{15}$N of $N_2$ in trapped air bubbles provide information about the thickness of the firn layer and past abrupt temperature changes that produce thermal gradients (Sowers et al., 1992; Schwander, 1989; Severinghaus et al., 1998). Because firn thickness is a function of accumulation rate and temperature, $\delta^{15}$N can be used to provide constraints on both variables through modeling of the firn densification process (Huber et al., 2006; Guillevic et al., 2013; Kindler et al., 2014). With independent constraints on the ice-core depth-age relationship, in particular from annual-layer counting, these approaches can be combined to produce robust estimates of temperature and accumulation rate through time. Results from Greenland (Buizert et al., 2014) and the West Antarctic Ice Sheet (WAIS) Divide ice core (Cuffey et al., 2016) provide recent examples.

In comparison with locations in West Antarctica and Greenland, ice-core sites in East Antarctica pose special challenges. The low accumulation rates typical of the East Antarctic plateau are less favorable for borehole thermometry; high accumulation rates and locations near ice divides, where horizontal velocities are low, are generally necessary for preservation of detectable thermal anomalies. Additionally, some recent studies have questioned the validity of firn models at the typically very cold temperatures during the glacial period in East Antarctica (Freitag et al., 2013; Bréant et al., 2017), since many of the models are calibrated with or designed for warmer conditions. One approach that may help to address such challenges is to use the "diffusion length," a measure of the spectral properties of high-depth-resolution measurements of water-isotope ratios. Water-isotope diffusion length reflects the vertical diffusion experienced by water molecules through the firn column (Johnsen, 1977; Whillans and Grootes, 1985; Cuffey and Steig, 1998; Johnsen et al., 2000). While diffusion length has primarily been used as a proxy for temperature (e.g., Simonsen et al., 2011; Gkinis et al., 2014; van der Wel et al., 2015; Holme et al., 2018; Gkinis et al., 2021), it is sensitive to both temperature and accumulation rate through their influence on the firn density profile and tortuosity, and is also affected by vertical strain (Gkinis et al., 2014; Jones et al., 2017a). Diffusion length thus provides an independent constraint on several important ice-core properties: temperature, accumulation rate, and the thinning history due to ice deformation.

Here, we present data from a new ice core (SPC14) from the South Pole, East Antarctica, and we use a novel approach to combine multiple data sets to constrain temperature, accumulation-rate, and ice-thinning histories. We take advantage of two timescales for SPC14, one for the ice (Winski et al., 2019) and one for the gas enclosed within it (Epifanio et al., 2020), to obtain an empirical measure of the gas-age ice-age difference ($\Delta$age). We also use high-resolution measurements of $\delta^{17}$O, $\delta^{18}$O, and $\delta$D of ice (Steig et al., 2021) to obtain water-isotope diffusion lengths.

We use a statistical inverse approach to obtain optimized, self-consistent reconstructions of temperature and accumulation rate using a combined firn-densification and water-isotope diffusion model. We exclude gas isotope ($\delta^{15}$N) data and use the water-isotope values only for calculating diffusion length, reserving these variables for comparison and validation. This approach allows us to produce a novel and independent calibration of the traditional isotope paleothermometer without the use of borehole thermometry. We also obtain an independent constraint on the thinning of annual layers. This is important at South Pole because the location of the site is about 200 km from the ice divide and the ice-flow history is not well known at ages earlier than the Holocene (Lilien et al., 2018).

## 2 Data from the South Pole Ice Core

The South Pole Ice Core (SPC14) was obtained from 2014 to 2016 at 89.9889°S, 98.1596°W, approximately 2 km from the geographic South Pole. SPC14 was drilled to a depth of 1751 m, equivalent to an age of approximately 54 ka (Winski et al., 2019). Compared to other East Antarctic plateau ice-core sites, South Pole has a relatively high annual accumulation rate (8 cm w.e. a$^{-1}$) (Casey et al., 2014) given its low mean-annual air temperature of -49°C (Lazzara et al., 2012). The mean firn temperature is -51°C (Severinghaus et al., 2001). The modern surface ice velocity is 10 m a$^{-1}$ (Casey et al., 2014).

The data sets used in our analysis are developed from the independent ice and gas timescales for SPC14 described previously by Winski et al. (2019) and Epifanio et al. (2020), respectively, and water-isotope measurements obtained at high depth resolution by continuous-flow analysis, as described in Steig et al. (2021). We briefly summarize the information obtained directly from the ice-core measurements as well as the data sets derived from that information (annual-layer thickness, $\Delta$age, and water-isotope diffusion length).

### 2.1 Ice Timescale and Annual-Layer Thickness

The SP19 ice timescale was constructed by stratigraphic matching of 251 volcanic tie points between SPC14 and WAIS Divide (Winski et al., 2019). Between tie points, identification of individual layers from seasonal cycles in sodium and magnesium ions was used to produce an annually-resolved timescale for most of the Holocene. For ages greater than 11.3 ka, despite lack of annual resolution, the uncertainty of the timescale is estimated to be within 124 years relative to WD2014 (Winski et al., 2019). Annual-layer thickness is given by the depth between successive years on the SP19 timescale. For ages older than 11.3 ka where annual layers could not be identified, Winski et al. (2019) found the smoothest annual-layer thickness which matched 95% of the volcanic tie points to within one year. Based on the uncertainty associated with interpolation between sparse tie points (Fudge et al., 2014), we estimate the uncertainty in annual-layer thickness (two standard deviations, hereafter s.d.) to be $\pm$3% of the value in the Holocene, increasing to $\pm$10% of the value at earlier ages.

### 2.2 Gas Timescale and Δage

Epifanio et al. (2020) developed the SPC14 gas timescale through stratigraphic matching of features in the high-resolution $CH_4$ records of the SPC14 and WAIS Divide cores. The difference in age between the ice and gas timescales, Δage, is a measure of the ice age at the lock-in depth, which depends on the rate of firn densification (Schwander and Stauffer, 1984; Schwander et al., 1988; Blunier and Schwander, 2000). Epifanio et al. (2020) determined Δage empirically at each of the $CH_4$ tie points and used a cubic spline fit to derive a continuous Δage curve for all depths. Due to the empirical nature of the gas timescale, the SPC14 Δage record is determined without the use of a firn-densification model. Moreover, the SPC14 Δage was obtained without relying on the additional constraint of $\delta^{15}$N to determine lock-in depth.

We assign an age to each empirical Δage estimate as the mid-point between the gas-age and ice-age timescales from which Δage is calculated. This approximation is justified by results from a dynamic densification model (Stevens et al., 2020), which show that at a site like South Pole the timescale on which Δage responds to climate variations is a time interval shorter than Δage itself. Uncertainty in Δage depends on uncertainty in the match between the WAIS Divide and SPC14 gas timescales, the uncertainty associated with interpolation between tie points, and uncertainty in the Δage for WAIS Divide. Because Δage is an order of magnitude smaller at WAIS Divide than at South Pole, that source of uncertainty is the smallest. The uncertainty estimated by Epifanio et al. (2020) ranges from ±1% to ±8% (two s.d.) of the value of Δage.

### 2.3 Water-Isotope Measurements and Diffusion Length

We measured water-isotope ratios at an effective resolution of 0.5 cm using continuous flow analysis (CFA), following the methods described in Jones et al. (2017b) and Steig et al. (2021). We measured $\delta^{18}$O and $\delta$D for the entirety of the core and $\delta^{17}$O from a depth of 556 m through the bottom of the core. We used Picarro Inc. cavity ring-down laser spectroscopy (CRDS) instruments, including both a model L2130-i (for $\delta^{18}$O and $\delta$D) and a model L2140-i for $\delta^{17}$O (Steig et al., 2014). We use the standard notation for $\delta^{18}$O:

$$\delta^{18}O_{sample} = \left(\frac{^{18}O}{^{16}O}\right)_{sample} \Big/ \left(\frac{^{18}O}{^{16}O}\right)_{VSMOW} - 1,$$

where VSMOW is Vienna Standard Mean Ocean Water. $\delta^{17}$O and $\delta$D are defined similarly. These measurements were used to calculate the water-isotope diffusion length. Figure 1 shows the $\delta^{18}$O measurements at 100-year-mean resolution as a function of age.

After deposition as snow on the ice-sheet surface, water isotopologues diffuse through interconnected air pathways among ice grains in the firn, driven by isotope-concentration gradients in the vapor phase (Johnsen, 1977; Whillans and Grootes, 1985; Cuffey and Steig, 1998). In solid ice below the firn column, diffusion continues, but at a rate orders of magnitude slower than in the firn (Johnsen et al., 2000). The extent of diffusion is quantified as the diffusion length, the mean cumulative diffusive-displacement in the vertical direction of water molecules relative to their original location in the firn.

Diffusion length is determined from spectral analysis of the high-resolution water-isotope data, following the methods described in Kahle et al. (2018). We use discrete data sections of 250 years. We calculate the diffusion length, $\sigma$, for each section by fitting its power spectrum with a model of a diffused power spectrum and a two-component model of the measurement system noise:

$$P = P_0 \exp(-k^2\sigma^2) + P_0' \exp(-k^2(\sigma')^2) + |\hat{\eta}|^2, \quad (1)$$

where $k$ is the wavenumber, $|\hat{\eta}|^2$ is the measurement noise, and $P_0$, $P_0'$, and $\sigma'$ are variable fitting parameters. The second term ($P_0' \exp(-k^2(\sigma')^2)$) accounts for the influence

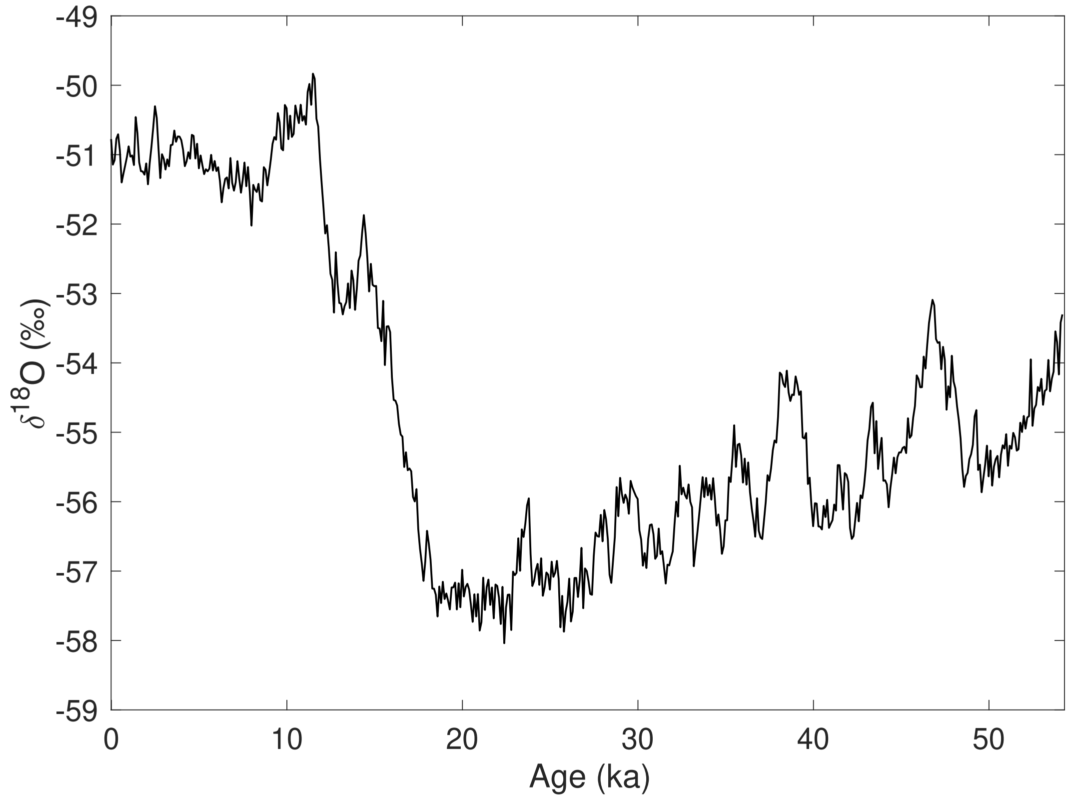


Figure 1: High-resolution $\delta^{18}$O record (Steig et al., 2021) from the South Pole ice core (SPC14), shown as discrete 100-year averages for clarity, on the SP19 ice timescale (Winski et al., 2019).

of the CFA measurement system on the water-isotope data spectrum. Kahle et al. (2018) found that this term does not completely eliminate the effect of system smoothing on the spectrum; we therefore make an additional correction, based on the sequential measurement of ice standards of known and differing isotopic composition, following Jones et al. (2017b). This correction is small, accounting for only ∼4% of the total diffusion length throughout the core. The uncertainty on $\sigma$ is estimated conservatively as described in Kahle et al. (2018) and varies from ±4% to ±66% (two s.d.) of the value throughout the core.

Additionally, we correct the diffusion-length estimates to account for diffusion in the solid ice, following Gkinis et al. (2014). This effect is also small, accounting for a maximum of 4% of the total diffusion length at the bottom of the core. To calculate the solid-ice diffusion length, we assume the modern borehole temperature profile $T(z)$ remains constant through time to find the diffusivity profile $D_{ice}(z)$, following Gkinis et al. (2014). We use borehole temperature measurements from the nearby neutrino observatory (Price et al., 2002). We assume a simple thinning function from a 1-D ice-flow model (Dansgaard and Johnsen, 1969) with a kink-height $h_0 = 0.2$ for this calculation; the error in this assumption is negligible for the small deviations in total thinning we are calculating. We subtract both the solid-ice and CFA diffusion lengths from the observations in quadrature to produce our final diffusion-length data set. Further details on both corrections are provided in the Supporting Information, Section S1.1.

We calculate the diffusion length for each of the three water-isotope ratios measured on the core. To combine the information from each isotope, we convert $\delta^{17}$O and $\delta$D diffusion lengths to equivalent values for $\delta^{18}$O. For example, the $\delta^{18}$O-equivalent diffusion length ($\sigma_{18\,from\,17}$) from the $\delta^{17}$O diffusion length ($\sigma_{17}$) is:

$$\sigma^2_{18\,from\,17} = \sigma^2_{17}\ \frac{D_{18}}{\alpha_{18}} \Big/ \frac{D_{17}}{\alpha_{17}}, \tag{2}$$

where $D$ and $\alpha$ are the corresponding air diffusivity and solid-vapor fractionation factor for each isotope. Values for $D$ and $\alpha$ are given in the Supporting Information, Section S1.2 (Majoube, 1970; Barkan and Luz, 2007; Luz and Barkan, 2010; Lamb et al., 2017). For the single diffusion-length record used in our analysis, we take the mean of these three estimates for $\sigma_{18}$.

## 3 Forward Model

We use a forward model to relate the observational data sets to the variables of interest. Figure 2 summarizes the data sets obtained from the ice-core measurements and the calculations described above: $\Delta$age, water-isotope diffusion length, and annual-layer thickness. We use these three data sets as our "observations" in a statistical inverse approach to infer temperature, accumulation rate, and ice-thinning function.

Figure 3 illustrates the structure of the forward model, including a firn-densification component, a water-isotope diffusion component, and a vertical strain (ice thinning) component. We describe the individual components below.

### 3.1 Firn Densification

The firn layer comprises the upper few tens of meters of the ice sheet where snow is progressively densifying into solid ice. As successive layers of snow fall on the surface of the ice sheet, the increase in overburden pressure causes the underlying ice crystals to pack closer together. The firn matrix densifies through this packing and through metamorphism of the crystal fabric. The rate of densification is determined primarily by temperature and accumulation rate. The Herron and Langway (1980) (HL) firn-densification model is a benchmark empirical model, based on depth-density data from Greenland and Antarctic ice cores (Lundin et al., 2017). We model the depth-density profile of the firn using the HL framework due to its simplicity and its good match with measurements of the modern South Pole firn density. We also evaluate the impact that using different firn models would have on our results (Section 5.1).

We use a surface density $\rho_0 = 350$ kg m$^{-3}$, consistent with measured values at the SPC14 site, and assume it remains constant through time (Fausto et al., 2018). We assess the sensitivity of our results to this assumption in Section 5.1. The bottom of the firn is constrained by a close-off density $\rho_{co}$, which we define as a function of temperature (Martinerie et al., 1994). As temperature varies between -50 and -60°C, close-off density varies in a small range between 831.5 and 836.4 kg m$^{-3}$.

We use the analytical formulation of the HL model, which assumes an isothermal firn. If either temperature or accumulation rate changes on short timescales, a transient formulation of the model would be required to reflect propagation through the firn column. Although our temperature and accumulation-rate inputs vary through time, the timescale of those variations (*i.e.,* 10 ka for ∼6°C change in temperature) is large enough that the steady-state approximation is acceptable. To test this assumption, we ran our forward model with a transient formulation of the HL model (Stevens et al., 2020) and found no difference in the results when we account for the advection time through the firn, as we do in our inverse approach. Since the transient model is more computationally expensive, we use the analytical formulation.

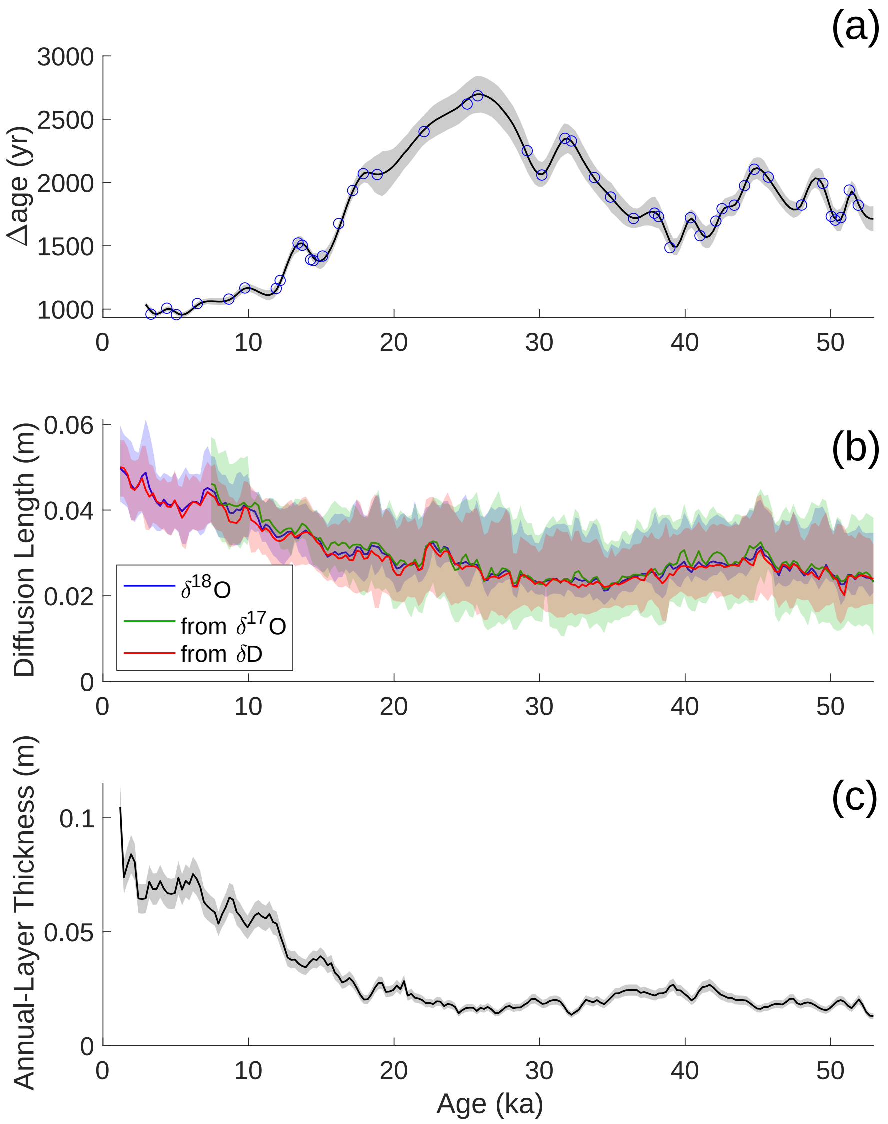


Figure 2: Data sets from SPC14 used to optimize the inverse problem, each averaged over bins of 250 years and plotted with uncertainty representing two s.d. Panel (a) shows Δage with tie points marked in blue circles, panel (b) shows water-isotope diffusion lengths, and panel (c) shows annual-layer thickness data. Diffusion lengths from $\delta^{17}$O (green) and $\delta$D (red) have been converted to $\delta^{18}$O-equivalent values.

### 3.2 Modeling Δage

Modeled Δage is given by the difference in the modeled age of the ice and the gas at the lock-in depth. We define the lock-in depth at a density of 10 kg m$^{-3}$ less than the close-

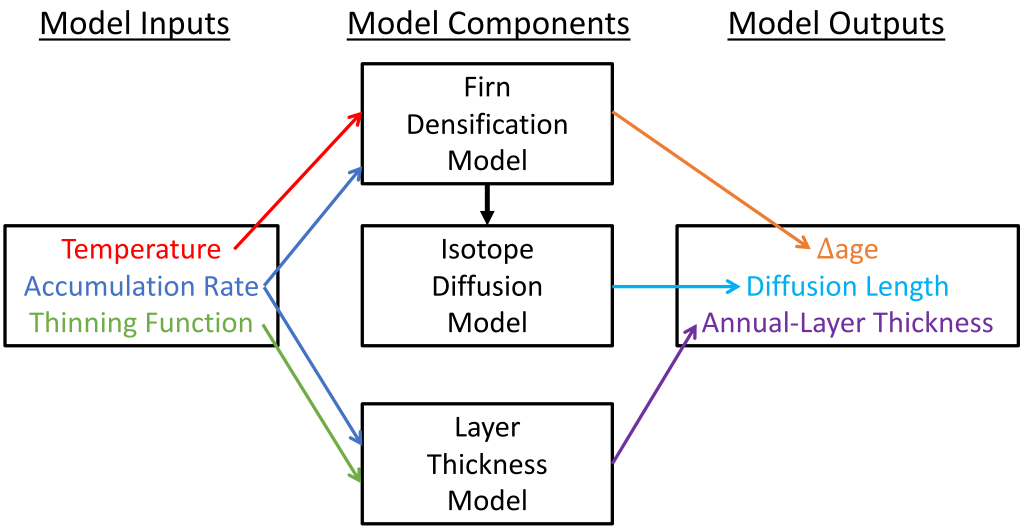


Figure 3: Illustration of the forward model components, which include firn densification (Section 3.1/3.2), water-isotope diffusion (Section 3.3), and a model of layer thickness (Section 3.4). Together, these components relate the variables of interest (temperature, accumulation rate, and thinning function) to the observational data sets (Δage, layer thickness, and diffusion length) shown in Figure 2.

off density (Blunier and Schwander, 2000). The age of the ice at this depth is estimated directly from the age-density profile from the firn-densification model. We estimate the age of the gas at the lock-in depth (LID) using the parameterization in Buizert et al. (2013):

$$\text{gas age}(\rho_{\text{LID}}) = \frac{1}{1.367}\left(0.934 \times \frac{(\text{DCH})^2}{D^0_{CO_2}} + 4.05\right), \tag{3}$$

where DCH is the diffusive column height given in units of m, defined as the lock-in depth minus a 3 m convective zone at the surface where firn air is well-mixed with the atmosphere. $D^0_{CO_2}$ is the free air diffusivity of $CO_2$ defined in Schwander et al. (1988) and Buizert et al. (2012) and given in units of m$^2$ a$^{-1}$. The lock-in depth is defined as the depth at which the effective molecular diffusivity of the gas is reduced to one thousandth of the free air diffusivity (Buizert et al., 2013).

### 3.3 Modeling Diffusion Length

The combined effects on the initial isotope profile ($\delta = \delta(z, 0)$) due to diffusion and firn densification are given by:

$$\frac{\partial \delta}{\partial t} = D\frac{\partial^2 \delta}{\partial z^2} - \dot{\epsilon} z \frac{\partial \delta}{\partial z}, \tag{4}$$

where $\delta(z', t)$ is the resulting smoothed and compressed isotope profile after time $t$ since deposition, $D$ is the diffusivity coefficient, $\dot{\epsilon}$ is the vertical strain rate, and $z$ is the vertical coordinate assuming an origin fixed on an arbitrary sinking layer of firn (Johnsen, 1977; Johnsen et al., 2000; Whillans and Grootes, 1985). Note that $z'$ accounts for the vertical compression of the original profile (Johnsen et al., 2000). Equation 4 is valid where the isotopic exchange between firn grains and the surrounding vapor is rapid, where the firn grains are well mixed and in isotopic equilibrium with the vapor, and where $\delta \ll 1000$‰.

The diffusivity coefficient $D_x$ of each isotope $x$ depends on the temperature and density profile of the firn column Whillans and Grootes (1985); Johnsen et al. (2000):

$$D_x = \frac{m\, p\, D_x^{air}}{RT\, \alpha_x\, \tau}\left(\frac{1}{\rho} - \frac{1}{\rho_{ice}}\right), \tag{5}$$

where $m$ is the molar weight of water, $p$ is the saturation pressure of water vapor over ice at temperature $T$ and with gas constant $R$, $D_x^{air}$ is the diffusivity of each isotopologue through air, $\alpha_x$ is the fractionation factor for each isotopic ratio in water vapor over ice, $\tau$ is the tortuosity of the firn, $\rho$ is the firn density, and $\rho_{ice}$ is the density of ice. Values for these parameters are given in the Supporting Information, Section S1.2.

Using the output from the firn-densification model, we calculate water-isotope diffusion through the depth-density profile. First, the density profile is used to calculate the diffusivity of each isotope based on Equation 5. We then solve for the diffusion length $\sigma_{firn}$ of a particular isotope ratio in terms of its effective diffusivity coefficient $D$ and the firn density $\rho$ (Gkinis et al., 2014):

$$\sigma_{firn}^2(\rho) = \frac{1}{\rho^2}\int_{\rho_0}^{\rho} 2\rho^2 \left(\frac{d\rho}{dt}\right)^{-1} D(\rho) d\rho, \tag{6}$$

where $\rho_0$ is the surface density and $\frac{d\rho}{dt}$ is the material derivative of the density. To calculate the diffusivity $D$, we use an atmospheric pressure of 0.7 atm, the ambient pressure at the SPC14 site (Severinghaus et al., 2001), which we assume to be constant through time.

Cumulative vertical strain significantly thins layers in the ice. The thinning function is defined as the fractional amount of thinning that has occurred at a given depth in the ice sheet. We account for the effects of vertical strain on our modeled firn diffusion length, $\sigma_{firn}$, using a thinning function $\Gamma$. We model the diffusion length measured in the ice core as $\sigma_{icecore}$:

$$\sigma_{icecore} = \sigma_{firn} \times \Gamma. \tag{7}$$

Recall that when we compare the modeled diffusion length with the observations, the observations have been corrected for diffusion in solid ice.

### 3.4 Modeling Annual-Layer Thickness

Annual-layer thickness $\lambda$ is given by the accumulation rate $\dot{b}$, in ice-equivalent m a$^{-1}$, multiplied by the thinning function $\Gamma$:

$$\lambda = \dot{b} \times \Gamma. \tag{8}$$

## 4 Inverse Framework and Results

### 4.1 Initialization

We use a Bayesian statistical approach to produce an ensemble of possible solutions to our inverse problem. Through many iterations, we use the forward model described above to solve our forward problem and determine the range of possible model inputs. This forward problem is described by the following equation, where the forward model, $G$, calculates the modeled observables, or data parameters, $d$ as a function of unknown input variables, or model parameters, $m$:

$$G(m) = d. \tag{9}$$

Our forward model $G$ is nonlinear and cannot be solved analytically. Instead, we use a Monte Carlo approach to solve the inverse problem by testing many instances of $m$ through the forward model $G$ to find the output $d$ that best matches the observations $d_{obs}$. The theory and practical implementation of this approach are detailed in the Supporting Information, Section S2 (Tarantola, 1987; Mosegaard and Tarantola, 1995; Gelman et al., 1996; Mosegaard, 1998; Khan et al., 2000; Mosegaard and Sambridge, 2002; Mosegaard and Tarantola, 2002; Steen-Larsen et al., 2010).

We incorporate *a priori* information about model parameters based on their modern values and our best estimate of how they have varied through time. We include this *a priori* information by creating bounds on the allowable model space to explore and use the Metropolis algorithm to randomly create perturbations that sample within the bounded model space (Metropolis et al., 1953). If the algorithm proposes a solution $m_x$ that falls outside of our bounded model space, $m_x$ is disregarded and another solution is evaluated. Because we expect the parameters to vary smoothly through time, proposed perturbations are smoothed with a lowpass filter to prevent spurious high-frequency noise from being introduced. Temperature and accumulation-rate perturbations are smoothed with a lowpass filter with a cutoff period of 3000 years, which corresponds to the maximum value of $\Delta$age and thus the limit of natural smoothing we expect from the ice-core data. We expect the thinning function to be even smoother and apply a lowpass filter with a cutoff period of 10,000 years to those perturbations.

We also determine initial guesses $m_1$ for each parameter. Initializing the problem at what is judged to be a reasonable solution $m_1$ helps to avoid non-physical solutions (MacAyeal, 1993; Gudmundsson and Raymond, 2008). We design initial guesses for each parameter that are simplified versions of our best initial guess, allowing higher-frequency information to be inferred from the optimization. The initial guess of temperature is a step-function version of the water-isotope record. The initial guess for the thinning function is the output of a Dansgaard and Johnsen (1969) (DJ) ice-flow model. This simple model produces an approximation of the dynamics acceptable at many ice-core sites (Hammer et al., 1978). We use a kink height of $h_0 = 0.2$ to simulate the flank flow at the SPC14 site. To produce an initial guess for accumulation rate, we divide the layer-thickness data by this thinning function and approximate the result with a simplified step function.

Each parameter is bounded based on naïve expectations for its variability. For temperature, we bound the model space with an upper and lower scaling of the step-function initial guess version of the water-isotope record. We create an envelope based on previous estimates of glacial-interglacial temperature change in Antarctica, which allows for solutions with glacial-interglacial changes as small as 0.5°C and as large as 15°C. For accumulation rate, the bounded model-parameter range is an envelope about our initial guess defined as $\pm 0.02$ m a$^{-1}$. Given the surface and Holocene accumulation-rate fluctuations at South Pole described in Lilien et al. (2018), this range is a reasonable limit on accumulation rate, while still allowing variation in the values tested in each $m$. For the ice-equivalent thinning function, we enforce a value of one at the surface but do not provide further constraints on the model space because it is effectively constrained by the bounds on accumulation rate and layer thickness.

### 4.2 *A posteriori* Distributions

The resulting solutions $m$ from our inverse approach are described by the *a posteriori* distribution. To visualize the high-dimensional *a posteriori* distribution, we plot probability distributions for each parameter. Rather than create separate probability distributions for each of the many parameters in our model space, we plot each probability distribution successively in a single figure to visualize the entire model space at once. Figure 4 shows our results, with the model inputs on the left and outputs on the right. The grey shading shows successive probability distributions. A vertical slice through the shading in each plot represents the probability distribution for a particular parameter (recall that a parameter represents the value of a variable at a specified model timestep, *e.g.,* the value of temperature at the 4th timestep). How often a particular value is accepted for each parameter is represented by the shading, where darker shading denotes values that were accepted more often. The solid magenta curves describe the initial guess for each parameter, and the dashed magenta curves describe the bounded model space (for temperature and accumulation rate). The right three panels of Figure 4 illustrate how well the modeled observables $d(m)$ match with the observations $d_{obs}$ throughout the collection of solutions.

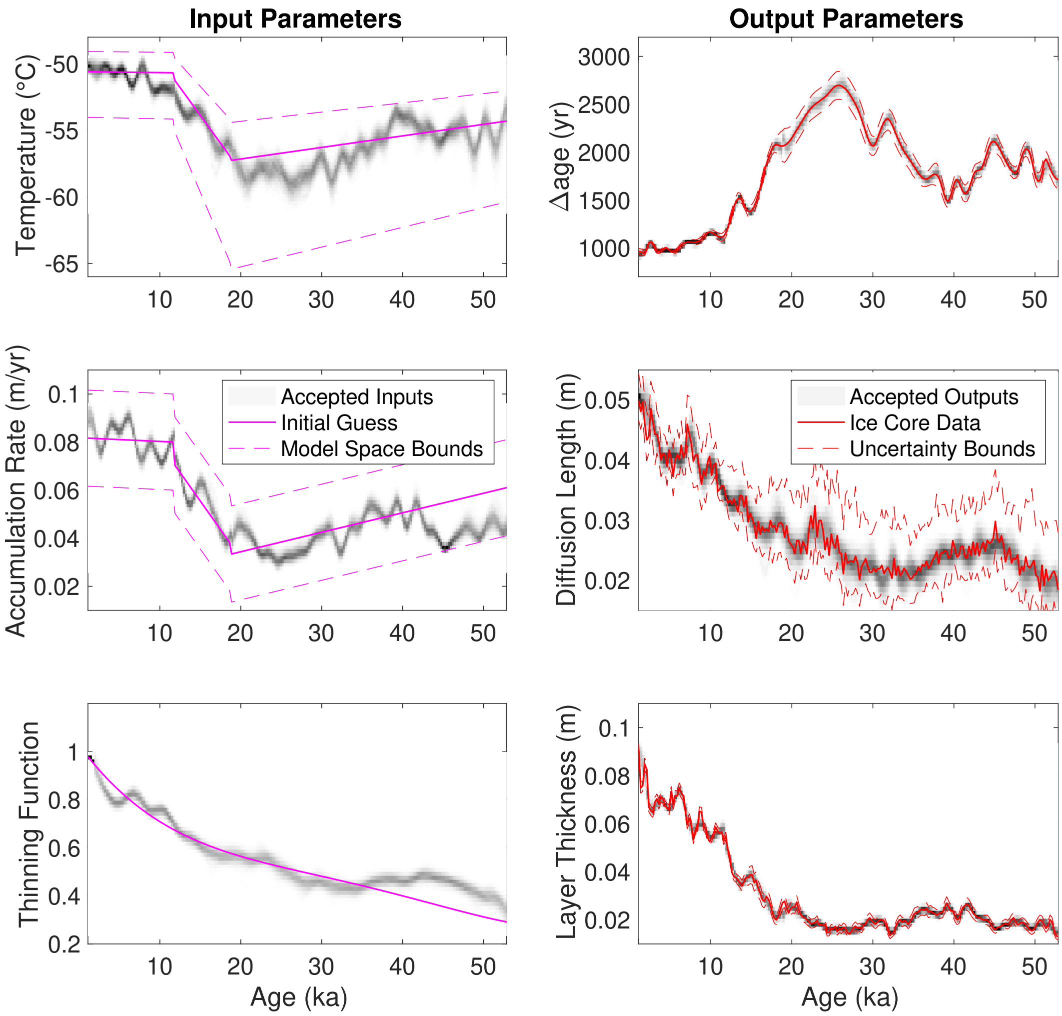


Figure 4: Results of the Monte Carlo inverse calculations, showing the *a posteriori* distribution result compared with *a priori* information. The grey shading in each panel represents probability distributions for each parameter from the *a posteriori* distribution, where darker shading signifies greater likelihood. Left panels show the initial guesses (solid magenta) and model bounds (dashed) for the input parameters: temperature, accumulation rate, and thinning. Right panels show the observational data (solid red) and prescribed uncertainties (dashed) for the output parameters: Δage, diffusion length, and layer thickness.

## 5 Sensitivity of Results

We evaluate the sensitivity of our results to choices within the forward model and inverse algorithm, as well as to constraints from the data sets included in the inverse problem and from independent data.

### 5.1 Sensitivity to Forward Model

Within the forward model, we hold the surface density $\rho_0$ in the firn-densification model constant through time. We tested two alternate values of surface density $\rho_0$ (450 kg m$^{-3}$ and 550 kg m$^{-3}$); we find no significant change in the results. We also did two experiments to assess the impact of the choice of firn-densification model. First, we evaluated the depth-density and age-density profiles using a large collection of models (Herron and Langway, 1980; Goujon et al., 2003; Ligtenberg et al., 2011; Simonsen et al., 2013; Li and Zwally, 2015) within the Community Firn Model framework (Stevens et al., 2020). Second, we implemented two of those models, those of Goujon et al. (2003) (GOU) and Ligtenberg et al. (2011) (LIG), within our inverse framework. The results are similar regardless of which firn model is used, but the GOU and LIG models produce consistently lower temperatures than the HL model. Because this difference is systematic throughout the depth of the core, the magnitude of reconstructed temperature variability, including the glacial-interglacial temperature change, is not significantly affected (Figures S3 and S4). Our choice of the HL model within our forward model is justified by the good agreement with modern temperature compared with these other models and the consistency within the interpretation of the temperature result across all models. Details from these sensitivity tests are given in the Supporting Information, Section S3.1. It has been suggested that most firn models (including the HL model) are biased to produce firn columns that are too thick at very cold temperatures (Landais et al., 2006; Dreyfus et al., 2010; Freitag et al., 2013; Bréant et al., 2017), though the magnitude of this bias is disputed. An implicit assumption in our method is that the HL model is unbiased. We discuss the implications of this assumption in Section 6.

### 5.2 Sensitivity to Inverse Algorithm

Within the formulation of the inverse algorithm, we evaluated the sensitivity to different initial guesses for each parameter. Altering the initial guesses within the model space bounds do not affect the final results. Additionally, including higher-frequency *a priori* information in our initial guesses does not change the results. For example, we evaluated initial guesses of constant values for each of temperature, accumulation rate, and thinning function. These extremely simplified initial guesses produce results indistinguishable from those that include the high-frequency variability of each comparison data set, but require many more iterations to reach an equilibrium solution. As recommended in Gudmundsson and Raymond (2008), we opted for a middle-ground approach that saves time by setting the initial guess close to the expected answer but relies on the optimization to obtain high-frequency information.

### 5.3 Sensitivity to Included Data Constraints

We also examined the sensitivity of the results to each data set individually, as detailed in the Supporting Information, Section S3.2. One key conclusion from these tests is that all three data sets ($\Delta$age, layer thickness, and diffusion length) provide important information for producing a well-constrained result (Figures S6 and S7), although the relative importance of each parameter varies with age in the record. In general, we find that the diffusion length and layer thickness are sufficient to constrain accumulation rate, and the $\Delta$age strongly impacts the temperature. However, while it is evident that $\Delta$age is the most important constraint on temperature for ages less than $\sim$35 ka, at greater ages, constraints provided by the combination of diffusion length and layer thickness become increasingly critical.

We also considered the influence of the temperature-dependence of water-isotope diffusivity. We evaluated the effect of removing the temperature-dependence (Equation 5), so that diffusion-length data affects only the thinning function (Equation 7), and temperature is primarily driven by the $\Delta$age data. The results show a significant difference from the main result, demonstrating that the diffusion-length data provide an important constraint on temperature, which has subsequent impact on other parameters. Further details are provided in the Supporting Information, Section S3.2.

### 5.4 Comparison with $\delta^{15}$N data

Finally, we consider the impact on our results of the inclusion of information from measurements of $\delta^{15}$N in $N_2$ of air bubbles in SPC14 (Winski et al., 2019; Severinghaus et al., 2019). The enrichment of $\delta^{15}$N in an ice core is a linear function of the original diffusive column height (DCH) of the firn, resulting from gravitational fractionation (Sowers et al., 1992; Buizert et al., 2013). We calculate DCH from $\delta^{15}$N as described in the Supporting Information (Equation S19). As shown in Figure S9, there are significant differences between the DCH calculated from the main reconstruction and that calculated from $\delta^{15}$N. We do not incorporate $\delta^{15}$N data in our full Monte-Carlo inverse procedure because this added constraint over-determines the solution; as we show in the following sensitivity test, no combinations of temperature and accumulation rate can simultaneously satisfy $\delta^{15}$N and the other data constraints at all depths in the core. Instead, we evaluate the impact of the additional constraint of $\delta^{15}$N data as follows.

We use the $\delta^{15}$N data to determine temperature and accumulation-rate pairs that produce a DCH in agreement with the $\delta^{15}$N-based DCH. To determine these pairs, we run a global search algorithm over a set of temperature and accumulation-rate values defined by a small range centered on the mean values from the main reconstruction (Figure 4). For each depth in the core, we use the HL firn model to calculate the DCH for all temperature and accumulation-rate values in the global search, and then select only the temperature and accumulation-rate pairs that produce a DCH within the uncertainty of the DCH calculated from $\delta^{15}$N. The result is shown in light-red shading in Figure 5. Compared with our main reconstruction, the accumulation-rate history remains essentially unchanged, but the mean temperature is greater by 2.8°C on average for the glacial period (*i.e.,* before about 15 ka). To further refine this suite of solutions, we select the subset of accumulation-rate and temperature values that both satisfy the $\delta^{15}$N constraint on DCH and are consistent (through the HL model) with $\Delta$age, within the uncertainty of the empirical $\Delta$age data. The blue shading in Figure 5 shows this combination of both $\delta^{15}$N and $\Delta$age constraints; the result is a decrease in mean values for both accumulation rate and temperature during the glacial period compared to $\delta^{15}$N alone. Areas of overlap (dark purple shading) between our main reconstruction and the combined $\delta^{15}$N and $\Delta$age constraints show where all constraints – diffusion length, layer thickness, $\Delta$age, $\delta^{15}$N – are satisfied. Further details on this sensitivity test are given in the Supporting Information, Section S3.3 and Figure S9.

Three important conclusions can be drawn from these comparisons. First, while our temperature and accumulation-rate reconstructions are entirely consistent with $\delta^{15}$N constraints during the Holocene, a combination of warmer temperatures and lower accumulation rates are required to match the $\delta^{15}$N constraint in the glacial period. Second, there is no consistent solution for which all constraints (layer thickness, diffusion length, $\Delta$age, and $\delta^{15}$N), for all depths in SPC14, are satisfied, implying that further refinements to firn models may be required (Supporting Information, Section S3.3). However, for those depths where all constraints are satisfied, the resulting temperatures are warmer by <1°C on average than in our main reconstruction. This means that, third, our results are conservative with respect to the assumption that the HL model produces the correct DCH at very cold temperatures. This also supports the exclusion of $\delta^{15}$N in our main reconstruction, to avoid giving too much weight to the reproduction of the DCH by the HL model. For this reason, we focus on the results from our main reconstruction in the discussion which follows.

## 6 Discussion

We now consider our main reconstructions for accumulation rate, ice thinning, and temperature in comparison with estimates from simpler calculations and independent data. In general, the results are in agreement with naïve expectations, but with some important differences. Because the accumulation-rate and thinning reconstructions are fun-

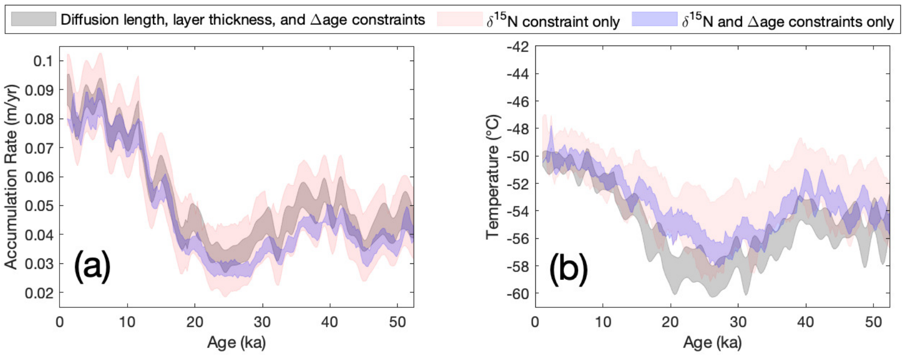


Figure 5: Results from a sensitivity test that includes $\delta^{15}$N as a constraint on diffusive column height (DCH). Panel (a) shows accumulation rate, and panel (b) shows temperature; shading represents 2 s.d. uncertainty for all three reconstructions. The main reconstruction is shown in grey. Results consistent with the $\delta^{15}$N constraints (only) are shown in red. Results consistent with both $\delta^{15}$N and the empirical $\Delta$age data are shown in blue. The overlap of blue and grey shows where all empirical constraints (layer thickness, diffusion length, $\Delta$age, and $\delta^{15}$N) are satisfied within the framework of the firn model. Further details are given in the Supporting Information, Section S3.3 and Figure S9.

damentally linked through Equation 8, we discuss them together. We then compare our reconstruction for temperature with the traditional water-isotope paleothermometer, and discuss the broader implications of our results. The *a posteriori* distribution is near-Gaussian, and in this section we plot its mean and standard deviation rather than the full probability distributions. Recall that the *a posteriori* distribution comprises only accepted solutions, a subset of all iterations.

## 6.1 Accumulation Rate and Thinning Function

Figure 6 shows the results for the thinning function (panel (a)) and accumulation rate (panel (b)). The grey shading denotes a band of two s.d. of the *a posteriori* distribution. In general, thinning functions are expected to be smooth and to decrease monotonically because they integrate the total thinning experienced at a given depth, as illustrated by the results of a 1-D Dansgaard-Johnsen (DJ) model with $h_0 = 0.2$ (red curve, panel (a)). However, the SPC14 site is far from an ice divide such that variations in the bed topography upstream can create more complex thinning histories (e.g., Parrenin et al., 2004). Thus, the thinning function result is similar to the DJ-model output, but contains additional higher-frequency variations. To evaluate the plausibility of these variations in the primary reconstruction, we compare with two other independent estimates of the thinning function, an ice-flow-model thinning function and a $\delta^{15}$N-based thinning function.

First, we compare the primary thinning function with one calculated from an ice-flow model. We use a 2.5-D flowband model (Koutnik et al., 2016) forced with observations of the bedrock topography and the accumulation-rate pattern. Details of the model setup are given in the Supporting Information, Section S4 (Nye, 1963; Looyenga, 1965; Gades et al., 2000; Neumann et al., 2008; Catania et al., 2010; Jordan et al., 2018). The resulting thinning function is best considered in two segments. The thinning function for the past 10 ka (solid black line in Figure 6) is well constrained because the flowline is known (Lilien et al., 2018) and the bed topography has been measured along the flowline (Figure S11). The key result is that the bed undulations along the flowline cause the same structure as is inferred in the primary thinning function. The "reversal" in the thinning function at 7 ka, where deeper layers have thinned less than shallower layers, matches

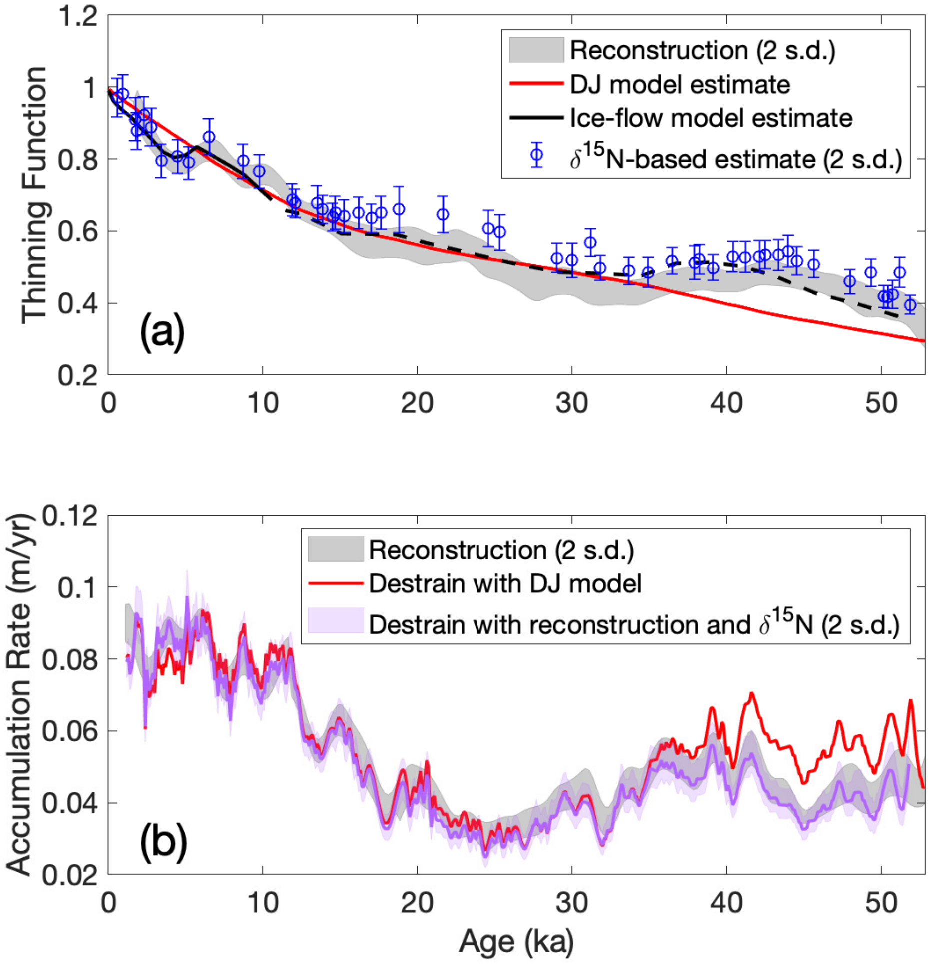


Figure 6: Reconstructions of accumulation rate and thinning function for SPC14. Two s.d. (grey shading) of the *a posteriori* distribution is plotted for each reconstruction alongside comparison estimates. Panel (a) shows the primary thinning function reconstruction (grey) compared to a DJ-model output with $h_0 = 0.2$ (red), an ice-flow-model thinning function from a 2.5-D flowband model (solid and dashed black), and a $\delta^{15}$N-based thinning function with error bars showing two s.d. uncertainty (blue). The solid black curve shows where the ice-flow-model thinning function is well constrained by data, and the dashed black curve shows where the bed topography is simulated. The thinning function is shown vs. depth in the Supporting Information (Figure S10). Panel (b) shows the accumulation-rate reconstruction compared to two versions of the destrained layer-thickness data. The thinning functions used for destraining are the DJ-model output (red) and the mean of the reconstruction and the $\delta^{15}$N-based estimate (purple).

well in both the primary and ice-flow-model thinning functions. This feature is caused by an overdeepening in the bed topography (Figure S18).

For ages older than 10 ka, we do not know where the ice originated and thus cannot use the ice-flow model to determine the thinning function with confidence. Instead, we aim to evaluate whether the primary thinning function is physically plausible, given what we know about the bed topography in the region. Using airborne radar measurements (Forsberg et al., 2017) to create a plausible bed beyond 100 km upstream, we show that the ice-flow model (black dashed line) can approximately match the magnitude and structure of the primary thinning function. Therefore, the primary thinning function is consistent with expectations, given plausible variations in bedrock topography.

Second, we compare the primary thinning function with a $\delta^{15}$N-based thinning function (blue circles; error bars show two s.d. uncertainty). We obtain this estimate following the methods described in Parrenin et al. (2012), who showed that the thinning function scales with the ratio of "$\Delta$depth" to the DCH, where $\Delta$depth is given by $\Delta$age multiplied by the depth/age slope from the ice-core timescale. The thinning function $\Gamma$ is then given by (Parrenin et al., 2012):

$$\Gamma = \frac{\Delta\text{depth}}{A \times \text{LID}}, \tag{10}$$

where $A$ is a scaling factor that accounts for the ice-equivalent thickness of the original firn column (Winski et al., 2019), and the lock-in depth, LID = DCH + 3, accounting for a 3-m convective zone. We use our temperature reconstruction to incorporate the impact of thermal fractionation in our calculation of the LID (Grachev and Severinghaus, 2003; Cuffey and Paterson, 2010; Fudge et al., 2019). Full details on this approach and its uncertainties are given in the Supporting Information, Section S5.

Figure 6a shows that the structure of the $\delta^{15}$N-based thinning function generally agrees with the primary reconstruction, showing the same high-frequency variations and mean estimates whose error bars in general overlap with the uncertainty of the primary reconstruction. There is the least agreement between ages of about 15 and 30 ka, where the $\delta^{15}$N-based thinning function is shifted appreciably towards higher values (less thinning). This is consistent with the observation that the modeled DCH from our main reconstruction tends to be higher than that calculated from $\delta^{15}$N. We note that the uncertainties for the $\Delta$depth calculation are not depth-independent; many known sources of error are expected to be systematic. For example, if the WAIS Divide $\Delta$age data set were systematically too large during the glacial period, correcting for this would result in smaller estimates for the SPC14 $\Delta$depth, and therefore smaller values (more thinning) in the $\delta^{15}$N-based thinning function. The same adjustment to $\Delta$age results in no significant change in the primary thinning function, thus improving the agreement between the means of the two independent estimates. We discuss further quantification of uncertainties in these calculations in Section 5.4 and Section S5.1 in the Supporting Information.

For comparison with the accumulation-rate reconstruction, Figure 6b shows two versions of high-frequency estimates produced by destraining the layer-thickness data with estimates of the thinning function. The red curve uses the 1-D Dansgaard-Johnsen thinning function; the resulting accumulation-rate estimate deviates from the reconstruction at the oldest ages. Thus, the reconstruction reflects a significantly smaller accumulation rate before 40 ka than would be inferred using a DJ model. The purple curve shows our best estimate for high-frequency accumulation rate by combining the information from both the primary thinning function and the $\delta^{15}$N-based thinning function; we use the mean of these two thinning functions to destrain the layer-thickness data. We incorporate information from both thinning functions in order to include all available information in our best estimate. The uncertainty is estimated by combining the uncertainties of both thinning functions.

### 6.2 Temperature Reconstruction

The temperature reconstruction is shown in Figure 7. For comparison, we show two scaled versions of the measured $\delta^{18}$O, corrected for secular variations in the $\delta^{18}$O of sea-water, following Bintanja and van de Wal (2008). Recall that while we used diffusion length determined from the $\delta^{18}$O power spectrum in our reconstruction, we do not use the abso-

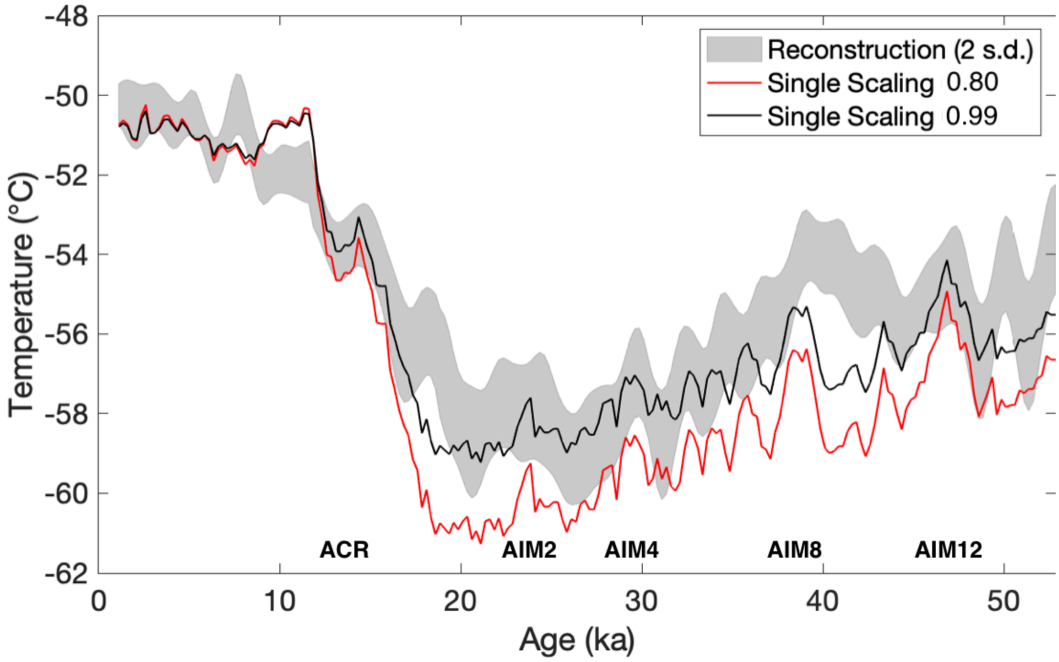


Figure 7: Reconstruction of temperature and relationship with $\delta^{18}$O. Grey shading shows two s.d. of the *a posteriori* distribution. Solid lines show scaled versions of $\delta^{18}$O, discretely averaged to 250-year resolution. The $\delta^{18}$O is scaled by 0.8‰°C$^{-1}$ (red), the modern surface relationship, and by 0.99‰°C$^{-1}$ (black), the calibrated linear relationship with the mean of the temperature reconstruction.

lute $\delta^{18}$O values; hence, these comparisons serve as an independent calibration of the traditional water-isotope thermometer, similar to what has been done previously with borehole thermometry (Cuffey et al., 1995, 2016) but maintaining higher-frequency information. The red curve in Figure 7 uses a scaling of $\partial(\delta^{18}\mathrm{O})/\partial T = 0.8$‰°C$^{-1}$, which is both the observed modern surface isotope-temperature relationship at the site (Fudge et al., 2020) and the value commonly used in the literature for Antarctica (e.g., Jouzel et al., 2003), for which Masson-Delmotte et al. (2008) report a 1 s.d. error of 0.01‰°C$^{-1}$. The black curve shows the best-fit linear calibration between $\delta^{18}$O and the mean of our reconstruction; this has a significantly greater slope of 0.99±0.03‰°C$^{-1}$ (2 s.d.). Our estimate of uncertainty on the slope accounts for errors in both variables, following the method of York et al. (2004), with errors on temperature given by the *a posteriori* distribution (Figure 7) and errors on $\delta^{18}$O (0.1‰, 1 s.d.) obtained from replicate continuous-flow measurements made on the South Pole ice core as reported in Steig et al. (2021). Results from the sensitivity tests (Section 5) using other firn models, and using independent $\delta^{15}$N constraints, yield the same result: slopes vary from 0.97 to greater than 1.2‰°C$^{-1}$. Correlation with the $\delta^{18}$O is greatest ($r$=0.94) with our main reconstruction (see Supporting Information, Section S3.4).

There are interesting similarities and differences between the calibrated $\delta^{18}$O and our independent temperature reconstruction. For example, the prominent Antarctic Isotope

Maximum 12 (AIM12) event, at about 47 ka, is similar in both our reconstruction and the scaled $\delta^{18}$O data, and suggests a temperature change of about 2°C. On the other hand, our temperature reconstruction for AIM8, at about 38 ka, is part of a low-frequency variation longer than that indicated by the $\delta^{18}$O data, and the mean reconstruction suggests that AIM8 was warmer than AIM12, while a simple linear scaling of the $\delta^{18}$O implies the opposite. Another interesting feature is AIM2 ($\sim$24 ka), which is muted in most East Antarctic records, but is prominent in the WAIS Divide ice core (WAIS Divide Project Members, 2013). AIM2 is clearly evident in both our reconstruction and in the scaled $\delta^{18}$O data, as is AIM4 ($\sim$30 ka) and the Antarctic Cold Reversal (ACR) ($\sim$13 ka).

In contrast, the early-Holocene isotope maximum (centered at about 10 ka) is muted in our temperature reconstruction. This is perhaps surprising, given the prevalence of this feature in the $\delta^{18}$O records, both at South Pole and elsewhere in East Antarctica. On the other hand, there is no early-Holocene peak in the WAIS Divide record, in either the $\delta^{18}$O or the borehole-calibrated temperature reconstruction (WAIS Divide Project Members, 2013; Cuffey et al., 2016). Furthermore, the temperature reconstruction suggests an earlier onset of deglacial warming (at about 22 ka) than the isotope data suggest, but similar to both the isotope data and the temperature reconstruction at WAIS Divide (WAIS Divide Project Members, 2013; Cuffey et al., 2016). Because large changes in the $\delta^{18}$O-temperature relationship can occur, for example, from changes in seasonality (Steig et al., 1994; Werner et al., 2000), we cannot assume that either result (*i.e.,*, our main reconstruction or the scaled $\delta^{18}$O) is the more faithful representation of temperature. Reconciling the differences would benefit from transient simulations, including water isotopes, of the AIM events and the early-Holocene maximum, as recently achieved for Dansgaard-Oeschger events in Greenland (Sime et al., 2019), and of the deglaciation.

Clearly, a single $\partial(\delta^{18}\mathrm{O})/\partial T$ scaling does not capture all of the variability in our temperature reconstruction. We explored calibrations separated by frequency and time period (*i.e.,* millennial versus glacial-interglacial frequencies and Holocene versus glacial time periods), but find the resulting fits were not statistically distinguishable from that of the single scaling. Thus, there is no evidence of the large change in scaling that has been observed in Greenland ice cores (Cuffey et al., 1995), attributable primarily to changes in the seasonality of precipitation (Steig et al., 1994; Werner et al., 2000). Our results agree well with the assumption generally made in East Antarctica that the slope remains constant through time (*e.g.,* Jouzel et al. (2003)), but show that this slope cannot be assumed to be the same as the modern spatial relationship.

While our calibration yields a significantly greater slope than has been generally used in previous work, this slope is consistent with isotope-modeling results. Modeling work has shown that the sensitivity of $\delta^{18}$O to temperature should increase at sites with colder mean-annual temperatures and higher elevations in Antarctica. For example, Markle (2017) obtains $\partial(\delta^{18}\mathrm{O})/\partial\ \mathrm{T} \sim 0.8‰°\mathrm{C}^{-1}$ for a location like WAIS Divide, in agreement with the borehole temperature calibration, and $\partial(\delta^{18}\mathrm{O})/\partial\ \mathrm{T} \sim 1‰°\mathrm{C}^{-1}$ for South Pole. This difference in sensitivity occurs because air masses traveling to higher elevations are on different moist isentropic surfaces and experience greater rainout for a given change in temperature (Bailey et al., 2019).

### 6.3 Upstream Corrections and Site Reconstructions

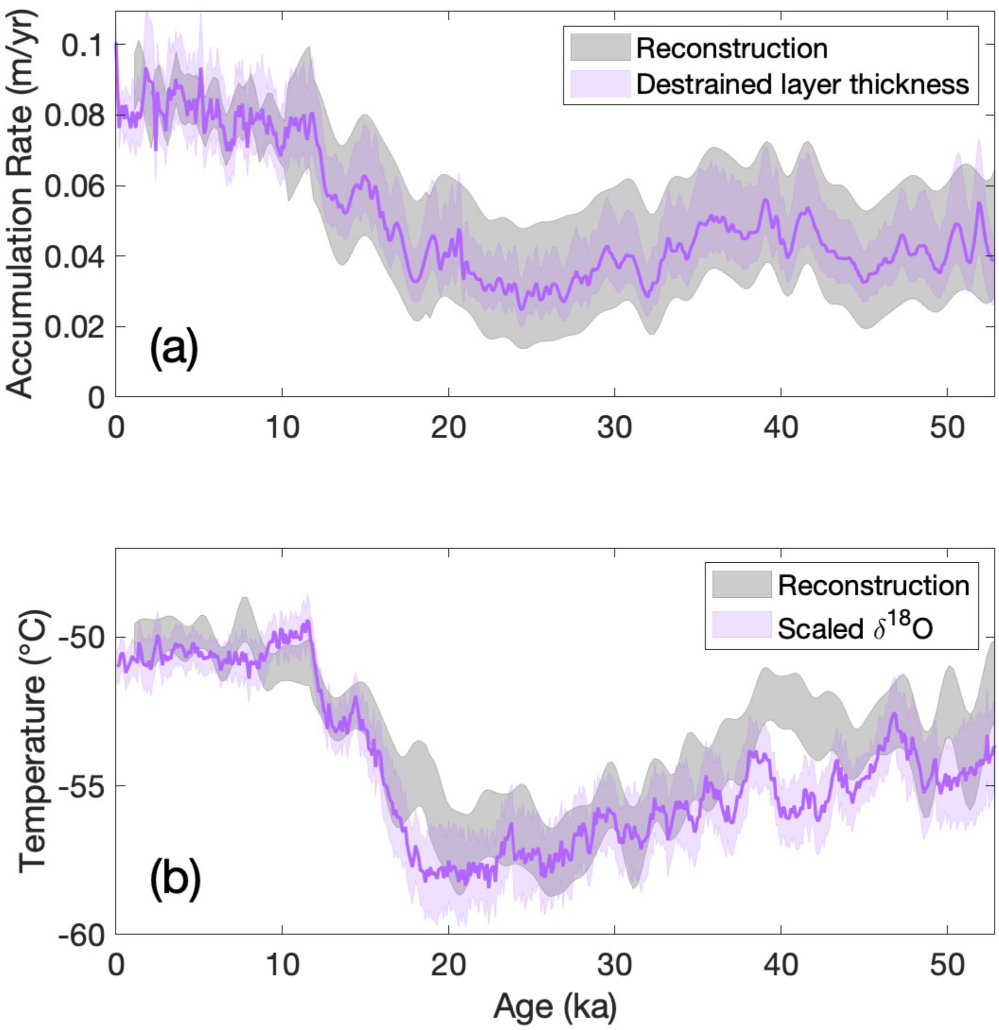


Figure 8: Advection-corrected reconstructions of accumulation rate and temperature at the South Pole site. Advection corrections are based on Lilien et al. (2018) and Fudge et al. (2020), as described in the text. All shading indicates two s.d. uncertainty. Panel (a) shows two advection-corrected accumulation-rate histories: the main reconstruction (grey) and the high-frequency accumulation-rate history from destraining 100-year average layer thicknesses (purple), corresponding to the ice-core histories shown in Figure 6b. Panel (b) compares the advection-corrected temperature estimates from our reconstruction and from the scaled $\delta^{18}$O, averaged to 100-year resolution. Uncertainty takes into account the correlation coefficient between the temperature reconstruction and the scaled isotope estimate.

Because SPC14 was drilled far from the divide, deeper ice in the core originated increasingly farther upstream. To obtain accurate climate histories, it is necessary to remove the influence of flow from upstream where the climate conditions are different. We correct for advection of ice based on Lilien et al. (2018) and Fudge et al. (2020). Using measurements of surface velocities and the pattern of modern accumulation rate upstream along the flowline, Lilien et al. (2018) correlated the measured ice-core layer thicknesses with the expected layer thickness due to advection through the upstream accumulation-rate pattern. This provides a unique constraint on the origin of ice for the past 10 ka and indicates an increase in surface flow speed of about 15% through that time period. We rely on this novel constraint for our advection correction rather than the advection predicted with the steady-state flowband model, and we note that the two approaches give similar trajectories for the reversal in the thinning function at 7 ka (Figure S13). Fudge et al. (2020) measured $\delta^{18}$O values using 10-m firn cores at 12.5 km intervals along the flowline to determine an appropriate correction for $\delta^{18}$O. Fudge et al. (2020) also measured 10-m firn temperatures, and while the results were inconclusive, they were consistent with a typical 10°C km$^{-1}$ lapse rate (dry adiabatic). Using this information, we apply corrections to the "ice core" reconstructions described above to produce "site" reconstructions of accumulation rate and temperature.

The upstream correction to accumulation rate is separated into two time intervals. For ages younger than 10.2 ka, the surface accumulation-rate pattern upstream of the core is known (Lilien et al., 2018). We apply these modern surface variations as a correction by adding the deviation from the mean value to the accumulation-rate ice-core reconstruction. This correction damps the variability of Holocene accumulation rate in the site reconstruction compared with the ice-core reconstruction, but it does not affect the trend of the mean. For ages older than 10.2 ka, there is an insignificant linear trend in the accumulation rate along the 100 km flowline such that Fudge et al. (2020) suggest no long-term advection correction. Thus we make no correction to the ice-core reconstruction for ages older than 10.2 ka. We do not attempt to correct for the impact of spatial variability on the ice-core reconstruction for these older ages, but note that non-climate variations of roughly 15% are expected to occur on millennial timescales. We estimate the uncertainty in the accumulation-rate upstream correction using the variations in accumulation rate along the flowline. For ages older than 10.2 ka, we assume the $1\sigma$ uncertainty is equal to the standard deviation of the upstream accumulation-rate pattern. For ages younger than 10.2 ka, the uncertainty is lower because we have removed much of the impact of advection; however, the correction is not perfect. Roughly 2/3 of the variance in the measured annual-layer thicknesses is explained by advection (Lilien et al., 2018). We thus conservatively assume a $1\sigma$ uncertainty is equivalent to half the standard deviation. Adding this uncertainty in quadrature to the uncertainty of the ice-core accumulation-rate estimates shown in Figure 6b, we produce the site accumulation-rate histories and their uncertainty bounds shown in Figure 8a. The grey bounds show the advection-corrected accumulation-rate reconstruction from our inverse approach and the purple bounds show the advection-corrected high-frequency accumulation-rate estimate from destraining the layer-thickness data with our thinning function reconstruction.

To correct the ice-core temperature reconstruction, we apply the dry adiabatic lapse rate of 10°C km$^{-1}$ to the elevation correction given by Fudge et al. (2020) to produce the grey shading in Figure 8b. We do not quantify uncertainty associated with this correction. For comparison with the water-isotope record, we correct the $\delta^{18}$O with the water-isotope correction given by Fudge et al. (2020) and scale the record using the best-fit linear calibration with the site reconstruction (also 0.99‰°C$^{-1}$) to produce the purple curve in Figure 8b. The uncertainty in the advection correction takes into account the correlation coefficient between the temperature reconstruction and the scaled isotope estimate.

We use our site temperature reconstruction to determine the magnitude of glacial-interglacial temperature change at South Pole. We define this change as the difference in the mean temperature within the intervals of 0.5 - 2.5 ka and 19.5 - 22.5 ka. Note that our reconstruction ends at 0.5 ka, not the present, because the upper ~500 years of the record is in the firn; hence, $\Delta$age is undefined and diffusion of water isotopes is still in progress.

The choice of the last glacial maximum (LGM) window avoids the prominent warming of the Antarctic Isotope Maximum (AIM2) event. The site temperature reconstruction gives a glacial-interglacial temperature change at the South Pole site of 6.65±0.96°C (one s.d.). The site scaled $\delta^{18}$O gives a glacial-interglacial temperature change of 7.15±0.68°C (one s.d.).

Our site temperature estimate indicates a 2 to 3.5°C lower glacial-interglacial surface temperature change than that reconstructed from other ice cores in east Antarctica, which is generally taken to be 9°C (Parrenin et al., 2013). Importantly, assessment of uncertainty in our calculations suggests that this key finding is conservative. In particular, there is some indication that firn-densification models may be biased to produce diffusive column heights that are too large at cold temperatures (Landais et al., 2006; Dreyfus et al., 2010; Freitag et al., 2013; Bréant et al., 2017). If the Herron-Langway model were in fact unbiased, then even warmer LGM temperatures would be required.

The difference between our results and the conventional 9°C value cannot be readily attributed to elevation change at South Pole, which is unlikely to have been more than 100 m thinner during the last glacial maximum, thus accounting for at most about 1°C of the difference, assuming a dry adiabatic lapse rate of 10°C km$^{-1}$. (Constraints from ice sheet models and geodetic data (Pollard and DeConto, 2009; Whitehouse et al., 2012; Briggs et al., 2014; Argus et al., 2014; Golledge et al., 2014; Roy and Peltier, 2015) show a near-zero mean elevation change, with a standard deviation of 50 m.)

Our results show that the commonly-used 9°C value for glacial-interglacial change in East Antarctica, which is based on water isotopes unconstrained by the independent estimates we use here, is too large. This finding may resolve an apparent disagreement, first recognized at least three decades ago (Crowley and North, 1991), between ice-core-based temperature estimates and results from general circulation models (GCMs), which produce cold-enough LGM temperatures only if surface elevations significantly higher than present are assumed (e.g., Masson-Delmotte et al., 2006; Lee et al., 2008; Werner et al., 2018), or other boundary conditions, such as extensive sea ice, are imposed (Schoenemann et al., 2014). Such GCM estimates are in better agreement with our results if corrected for the prescribed elevation changes, consistent with the smaller changes in East Antarctic ice elevations during the LGM indicated by more recent results than those suggested by earlier work (e.g., Peltier, 2004).

## 7 Conclusions

The South Pole ice core (SPC14) provides the opportunity to obtain reconstructions of important climate variables using multiple independent constraints. SPC14 has an empirical measure of the gas-age ice-age difference, $\Delta$age, obtained independently of firn-densification modeling (Epifanio et al., 2020). We also present a new continuous record of water-isotope diffusion length. Both $\Delta$age and diffusion length depend on firn properties, which in turn depend on the snow-accumulation rate and firn temperature. The water-isotope diffusion length provides an important additional constraint on the ice-thinning function, which relates measured layer thickness with the original accumulation rate at the surface. Layer thickness variations in SPC14 are well constrained by the ice timescale for the core, developed by annual-layer counting through the Holocene and by stratigraphic matches with the well-dated West Antarctic Ice Sheet Divide ice core (Winski et al., 2019). We have used a statistical inverse approach to combine information from all these data sets to obtain an ensemble of self-consistent temperature, accumulation-rate, and ice-thinning histories.

Our estimate of the thinning function for SPC14 indicates greater variations in thinning rate, in particular less thinning at depth, than can be captured with a simple one-dimensional ice-flow parameterization such as the commonly-used Dansgaard-Johnsen model. Variations in thinning comparable in timing and magnitude to our results are supported by a 2.5-D flowband model that accounts for variations in bedrock topography upstream of the drill site. The thinning function reconstruction is particularly important because SPC14 was drilled more than 200 km away from the ice divide and the surface velocity is high (10 m $a^{-1}$) (Casey et al., 2014). Our results demonstrate the value of using water-isotope diffusion length, in conjunction with annual-layer thickness, to more precisely constrain the thinning function. This approach, also employed by Gkinis et al. (2014) for a Greenland ice core, is entirely independent of the $\delta^{15}$N method of Parrenin et al. (2012), and provides an important new observational constraint on ice-sheet flow.

Our temperature reconstruction serves two important purposes. First, it provides the first empirical, high-frequency estimate of temperature for an East Antarctic ice-core site that does not depend on the traditional water-isotope paleothermometer. It thus enables an independent calibration of the isotope-temperature sensitivity, $\partial(\delta^{18}\mathrm{O})/\partial T$, similar to what has been done in central Greenland and in West Antarctica using borehole thermometry (Cuffey et al., 1995, 2016). Moreover, our approach preserves additional high-frequency information that is not available from the highly diffused borehole-temperature measurements. We find no evidence of a time- or frequency-dependence to the $\partial(\delta^{18}\mathrm{O})/\partial T$ relationship, in contrast to the case for Greenland. Second, our results indicate a smaller glacial-interglacial temperature change at South Pole than previously estimated elsewhere in East Antarctica. Our results yield a glacial-interglacial change of 6.7±1.0°C (one s.d.). This value is in better agreement with results from climate models, which generally match the much colder LGM temperatures obtained from traditional isotope-temperature scaling only when high ice-sheet elevations are assumed. The difficulty of reconciling temperature estimates from climate models and ice-core data has been noted in the literature for more than three decades (Crowley and North, 1991; Masson-Delmotte et al., 2005; Lee et al., 2008; Schoenemann et al., 2014). Our results thus lend greater confidence to the fidelity of climate-model simulations of last glacial maximum climate.

## 8 Data Availability

The published data set associated with this paper, including water isotope diffusion lengths and all of the reconstructions discussed in this manuscript, can be accessed through the USAP Data Center (DOI: 10.15784/601396). The SPC14 high-resolution water stable isotope record published with this paper can also be accessed through the USAP Data Center (DOI: 10.15784/601239). The radar data used in the ice-flow modeling can be accessed through the USAP Data Center at https://www.usap-dc.org/view/project/p0000200. The code used in this work is publicly available at https://doi.org/10.5281/zenodo.4579416, and the Community Firn Model is available at https://doi.org/10.5281/zenodo.3585885.

## Acknowledgments

This work was funded through grants from the US National Science Foundation (E.J.S. (1143105 and 1141839), C.B. (1643394 and 1443472), M.R.K. and others (1443471)). We thank J.P. Severinghaus for providing $^{15}$N data collected under grant NSF1443710. We thank G.H. Roe, B.R. Markle, and D. Shapero for suggestions on this work, and M. Twickler and J. Souney for their work administering the SPICEcore project. We thank the SPICEcore field team, the 109th New York Air National Guard, and the National Science Foundation Ice Core Facility, for the collection, transport, processing, and storage of the core. Finally, we thank the two reviewers of this manuscript for their very thorough comments and suggestions, which helped considerably in compiling the final publication.

## References

Argus, D. F., Peltier, W. R., Drummond, R. & Moore, A. W. (2014). The Antarctica component of postglacial rebound model ICE-6G C (VM5a) based upon GPS positioning, exposure age dating of ice thicknesses, and relative sea level histories. *Geophys. J. Int., 198*(1), 537–563. https://doi.org/10.1093/gji/ggu140

Bailey, A., Singh, H. K. A., & Nusbaumer, J. (2019). Evaluating a moist isentropic rramework for poleward moisture transport: implications for water isotopes over Antarctica. *Geophysical Research Letters, 46*(13), 7819–7827. https://doi.org/10.1029/2019GL082965

Barkan, E., & Luz, B. (2007). Diffusivity fractionations of $H_2^{16}O/H_2^{17}O$ and $H_2^{16}O/H_2^{18}O$ in air and their implications for isotope hydrology. *Rapid Communications in Mass Spectrometry, 21*(18), 2999–3005. https://doi.org/10.1002/rcm.3180

Bazin, L., Landais, A., Lemieux-Dudon, B., Toyé Mahamadou Kele, H., Veres, D., Parrenin, F., et al. (2013). An optimized multi-proxy, multi-site Antarctic ice and gas orbital chronology (AICC2012): 120–800 ka. *Climate of the Past, 9*, 1715–1731. https://doi.org/10.5194/cp-9-1715-2013

Bintanja, R., & van de Wal, R. S. W. (2008). North American ice-sheet dynamics and the onset of 100,000-year glacial cycles. *Nature, 454*(7206), 869–872. https://doi.org/10.1038/nature07158

Blunier, T., & Schwander, J. (2000). Gas enclosure in ice: age difference and fractionation. *Physics of Ice Core Records* 307–326. Hokkaido University Press.

Bréant, C., Martinerie, P., Orsi, A., Arnaud, L., & Landais, A. (2017). Modelling firn thickness evolution during the last deglaciation: constraints on sensitivity to temperature and impurities. *Climate of the Past, 13*, 833–853. https://doi.org/10.5194/cp-13-833-2017

Briggs, R. D., Pollard, T., & Tarasov, L. (2014). A data-constrained large ensemble analysis of Antarctic evolution since the Eemian. *Quaternary Science Reviews, 103*, 91–115. https://doi.org/10.1016/j.quascirev.2014.09.003

Buizert, C., Martinerie, P., Petrenko, V. V., Severinghaus, J. P., Trudinger, C. M., Witrant, E., Steele, L. P., et al. (2012). Gas transport in firn: multiple-tracer characterisation and model intercomparison for NEEM, Northern Greenland. *Atmospheric Chemistry and Physics, 12*(9), 4259–4277. https://doi.org/10.5194/acp-12-4259-2012

Buizert, C., Sowers, T., & Blunier, T. (2013). Assessment of diffusive isotopic fractionation in polar firn, and application to ice core trace gas records. *Earth and Planetary Science Letters, 361*, 110–119. https://doi.org/10.1016/j.epsl.2012.11.039

Buizert, C., Gkinis, V., Severinghaus, J. P., He, F., Lecavalier, B. S., Kindler, P., Brook, E. J., et al. (2014). Greenland temperature response to climate forcing during the last deglaciation. *Science, 345*(6201), 1177–1180. https://doi.org/10.1126/science.1254961

Buizert, C., Cuffey, K. M., Severinghaus, J. P., Baggenstos, D., Fudge, T. J., Steig, E. J., Sowers, T. A., et al. (2015). The WAIS divide deep ice core WD2014 chronology–Part 1: methane synchronization (68–31 kaBP) and the gas age–ice age difference. *Climate of the Past, 11*, 153–173. https://doi.org/10.5194/cp-11-153-2015

Casey, K. A., Fudge, T. J., Neumann, T. A., Steig, E. J., Cavitte, M. G. P., & Blankenship, D. D. (2014). The 1500 m South Pole ice core: Recovering a 40 ka environmental record. *Annals of Glaciology, 55*(68), 137–146. https://doi.org/10.3189/2014AoG68A016

Catania, G, C. Hulbe, & Conway, H. (2010). Grounding-line basal melt rates determined using radar-derived internal stratigraphy. *Journal of Glaciology, 56*(197), 545–554. https://doi.org/10.3189/002214310792447842

Crowley, T. J., & North, G. R. (1991). *Paleoclimatology.* New York, NY: Oxford University Press.

Cuffey, K. M., & Steig, E. J. (1998). Isotopic diffusion in polar firn: Implications for interpretation of seasonal climate parameters in ice-core records, with emphasis on central Greenland. *Journal of Glaciology, 44*(147), 273–284.

https://doi.org/10.3189/S0022143000002616
Cuffey, K. M., & Paterson, W. S. B. (2010). The physics of glaciers. Academic Press.
Cuffey, K. M., Clow, G. D., Alley, R. B., Stuiver, M., Waddington, E. D., & Saltus, R. W. (1995). Large arctic temperature change at the Wisconsin-Holocene glacial transition. *Science, 270*(5235), 455–458. https://doi.org/10.1126/science.270.5235.455
Cuffey, K. M., Clow, G. D., Steig, E. J., Buizert, C., Fudge, T. J., Koutnik, M., Severinghaus, J. P., et al. (2016). Deglacial temperature history of West Antarctica. *Proceedings of the National Academy of Sciences, 113*(50), 14249–14254. https://doi.org/10.1073/pnas.1609132113
Dahl-Jensen, D., Mosegaard, K., Gundestrup, N., Clow, G. D., Johnsen, S. J., Hansen, A. W., & Balling, N. (1998). Past temperatures directly from the Greenland ice sheet. *Science, 282*(5387), 268–271. https://doi.org/10.1126/science.282.5387.268
Dansgaard, W. (1964). Stable isotopes in precipitation. *Tellus B, 16*(4), 436–468. https://doi.org/10.3402/tellusa.v16i4.8993
Dansgaard, W., & Johnsen, S. J. (1969). A flow model and a time scale for the ice core from Camp Century, Greenland. *Journal of Glaciology, 8*(53), 215–223. https://doi.org/10.3189/S0022143000031208
Dreyfus, G. B., Jouzel, J., Bender, M. L., Landais, A., Masson-Delmotte, V., & Leuenberger, M. (2010). Firn processes and $\delta^{15}$N: potential for a gas-phase climate proxy. *Quaternary Science Reviews, 29*(1-2), 28-42. https://doi.org/10.1016/j.quascirev.2009.10.012
Epifanio, J. A., Brook, E. J., Buizert, C., Edwards, J. S., Sowers, T. A., Kahle, E. C., Severinghaus, J. P., Steig, E. J., Winski, D. A., Osterberg, E. C., Fudge, T. J., Aydin, M., Hood, E., Kalk, M., Kreutz, K. J., Ferris, D. G., & Kennedy, J. A. (2020). The SP19 chronology for the South Pole Ice Core–Part 2: gas chronology, $\Delta$age, and smoothing of atmospheric records. *Climate of the Past, 16*(6), 2431–2444. https://doi.org/10.5194/cp-16-2431-2020
EPICA Community Members. 2004. Eight glacial cycles from an Antarctic ice core. *Nature, 429*, 623–628. https://doi.org/10.1038/nature02599
Fausto, R. S., Box, J. E., Vandecrux, B. R. M., van As, D., Steffen, K., MacFerrin, M. J., Charalampidis, C., et al. (2018). A snow density dataset for improving surface boundary conditions in Greenland ice sheet firn modeling. *Frontiers in Earth Science, 6*, 51. https://doi.org/10.3389/feart.2018.00051
Forsberg, R., Olesen, A. V., Ferraccioli, F., Jordan, T., Corr, H., & Matsuoka, K. (2017). PolarGap 2015/16: Filling the GOCE polar gap in Antarctica and ASIRAS flight around South Pole. Radar grids available at: *ftp://ftp.bas.ac.uk/tomj/PolarGAP/PolarGAP_radar_grids.zip*
Freitag, J., Kipfstuhl, S., Laepple, T., & Wilhelms, F. (2013). Impurity-controlled densification: a new model for stratified polar firn. *Journal of Glaciology, 59*(218), 1163–1169. https://doi.org/10.3189/2013JoG13J042
Fudge, T. J., Waddington, E. D., Conway, H., Lundin, J. M. D., & Taylor, K. (2014). Interpolation methods for Antarctic ice-core timescales: application to Byrd, Siple Dome and Law Dome ice cores. *Climate of the Past, 10*(3), 1195–1209. https://doi.org/10.5194/cp-10-1195-2014
Fudge, T. J., Markle, B. R., Cuffey, K. M., Buizert, C., Taylor, K. C., Steig, E. J., Koutnik, M., et al. (2016). Variable relationship between accumulation and temperature in West Antarctica for the past 31,000 years. *Geophysical Research Letters, 43*(8), 3795–3803. https://doi.org/10.1002/2016GL068356
Fudge, T. J., Biyani, S. C., Clemens-Sewall, D., & Hawley, R. L. (2019). Constraining geothermal flux at coastal domes of the Ross Ice Sheet, Antarctica. *Geophysical Research Letters, 46*(22), 13090–13098. https://doi.org/10.1029/2019GL084332

Fudge, T. J., Lilien, D. A., Koutnik, M., Conway, H., Stevens, C. M., Waddington, E. D., Steig, E. J., Schauer, A. J., & Holschuh, N. (2020). Advection and non-climate impacts on the South Pole Ice Core. *Climate of the Past, 16*, 819–832. https://doi.org/10.5194/cp-16-819-2020

Gades, A. M., Raymond, C. F., Conway, H., & Jacobel, R. W., (2000). Bed properties of Siple Dome and adjacent ice streams West Antarctica, inferred from radio-echo sounding measurements. *Journal of Glaciology, 46*(152), 88–94. https://doi.org/10.3189/172756500781833467

Gelman, A., Roberts, G. & Gilks W. (1996). Efficient Metropolis jumping rules, in Bayesian Statistics 5, Berger, J. O., Bernardo, J. M., Dawid, A. P. and Smith, A. F. M. (eds), Oxford University Press.

Gkinis, V., Simonsen, S. B., Buchardt, S. L., White, J. W. C., & Vinther, B. M. (2014). Water isotope diffusion rates from the NorthGRIP ice core for the last 16,000 years - glaciological and paleoclimatic implications. *Earth and Planetary Science Letters, 405*, 132–141. https://doi.org/10.1016/j.epsl.2014.08.022

Gkinis, V., Holme, C., Kahle, E.C., Stevens, C.M., Steig, E.J., & Vinther, B.M. (2021). Numerical experiments on firn isotope diffusion with the Community Firn Model. *Journal of Glaciology, 67*(263), 450-472. https://doi.org/10.1017/jog.2021.1

Golledge, N. R., Menviel, L., Carter, L., Fogwill, C. J., England, M. H., Cortese, G., & Levy, R. H. (2014). Antarctic contribution to meltwater pulse 1A from reduced Southern Ocean overturning. *Nature Communications, 5*(1), 1–10. https://doi.org/10.1038/ncomms6107

Goujon, C., Barnola, J. M., & Ritz, C. (2003). Modeling the densification of polar firn including heat diffusion: Application to close-off characteristics and gas isotopic fractionation for Antarctica and Greenland sites. *Journal of Geophysical Research: Atmospheres, 108*(D24). https://doi.org/10.1029/2002JD003319

Grachev, A. M., & Severinghaus, J. P. (2003). Laboratory determination of thermal diffusion constants for $^{29}N_2/^{28}N_2$ in air at temperatures from 60 to 0 C for reconstruction of magnitudes of abrupt climate changes using the ice core fossil–air paleothermometer. *Geochimica et Cosmochimica Acta, 67*(3), 345–360. https://doi.org/10.1016/S0016-7037(02)01115-8

Gudmundsson, G. H., & Raymond, M. (2008). On the limit to resolution and information on basal properties obtainable from surface data on ice streams. *The Cryosphere, 2*(3), 413–445. https://doi.org/10.5194/tc-2-167-2008

Guillevic, M., Bazin, L., Landais, A., Kindler, P., Orsi, A., Masson-Delmotte, V., Martinerie, P., et al. (2013). Spatial gradients of temperature, accumulation and $\delta^{18}$O-ice in Greenland over a series of Dansgaard-Oeschger events. *Climate of the Past, 9*(3), 1029–1051. https://doi.org/10.5194/cp-9-1029-2013

Hammer, C. U., Clausen, H. B., Dansgaard, W., Gundestrup, N., Johnsen, S. J., & Reeh, N. (1978). Dating of Greenland ice cores by flow models, isotopes, volcanic debris, and continental dust. *Journal of Glaciology, 20*(82), 3–26. https://doi.org/10.3189/S0022143000021183

Herron, M. M., & Langway, C. C. (1980). Firn densification: an empirical model. *Journal of Glaciology, 25*(93), 373–385. https://doi.org/10.3189/S0022143000015239

Holme, C., Gkinis, V., & Vinther, B. M. (2018). Molecular diffusion of stable water isotopes in polar firn as a proxy for past temperatures. *Geochimica et Cosmochimica Acta, 225*, 128–145. https://doi.org/10.1016/j.gca.2018.01.015

Huber, C., Leuenberger, M., Spahni, R., Flückiger, J., Schwander, J., Stocker, T. F., Jouzel, J., et al. (2006). Isotope calibrated Greenland temperature record over Marine Isotope Stage 3 and its relation to $CH_4$. *Earth and Planetary Science Letters, 243*(3-4), 504–519. https://doi.org/10.1016/j.epsl.2006.01.002

Johnsen, S. J. (1977). Stable isotope homogenization of polar firn and ice, in *Proc. of Symp. on Isotopes and Impurities in Snow and Ice*, pp. 210–219, Int. Assoc. of Hydrol. Sci., Gentbrugge, Belgium.

Johnsen, S. J., Clausen, H. B., Cuffey, K. M., Hoffmann, G., Schwander, J., & Creyts, T. (2000). Diffusion of stable isotopes in polar firn and ice: The isotope effect in firn diffusion. T. Hondoh (Ed.), *Physics of Ice Core Records*, Hokkaido University Press, Sapporo (2000), pp. 121–140.

Jones, T. R., Cuffey, K. M., White, J. W. C., Steig, E. J., Buizert, C., Markle, B. R., McConnell, J. R., & Sigl, M. (2017a). Water isotope diffusion in the WAIS Divide ice core during the Holocene and last glacial. *Journal of Geophysical Research: Earth Surface, 122*(1), 290–309. https://doi.org/10.1002/2016JF003938

Jones, T. R., White, J. W. C., Steig, E. J., Vaughn, B. H., Morris, V., Gkinis, V., Markle, B. R., & Schoenemann, S. W. (2017b). Improved methodologies for continuous flow analysis of stable water isotopes in ice cores. *Atmospheric Measurement Techniques, 10*, 617–632. https://doi.org/10.5194/amt-10-617-2017

Jordan, T. A., Martin, C., Ferraccioli, F., Matsuoka, K., Corr, H., Forsberg, R., Olesen, A., & Siegert, M. (2018). Anomalously high geothermal flux near the South Pole. *Scientific Reports, 8*(1), 1–8. https://doi.org/10.1038/s41598-018-35182-0

Jouzel, J., Barkov, N. I., Barnola, J. M., Bender, M., Chappellaz, J., Genthon, C., Raynaud, D., et al. (1993). Extending the Vostok ice-core record of palaeoclimate to the penultimate glacial period. *Nature, 364*(6436), 407–412. https://doi.org/10.1038/364407a0

Jouzel, J., Vimeux, F., Caillon, N., Delaygue, G., Hoffmann, G., Masson-Delmotte, V., & Parrenin, F. (2003). Magnitude of isotope/temperature scaling for interpretation of central Antarctic ice cores. *Journal of Geophysical Research: Atmospheres*, 108(D12). https://doi.org/10.1029/2002JD002677

Jouzel, J., Masson-Delmotte, V., Cattani, O., Dreyfus, G., Falourd, S., Hoffmann, G., Fischer, H., et al. (2007). Orbital and millennial Antarctic climate variability over the past 800,000 years. *Science, 317*(5839), 793–796. https://doi.org/10.1126/science.1141038

Kahle, E. C., Holme, C., Jones, T. R., Gkinis, V., & Steig, E. J. (2018). A generalized approach to estimating diffusion length of stable water isotopes from ice-core data. *Journal of Geophysical Research: Earth Surface, 123*(10), 2377–2391. https://doi.org/10.1029/2018JF004764

Kahle, E. C. (2020). Climate reconstructions from ice cores: New techniques to understand the information preserved in the South Pole ice core (Doctoral dissertation, University of Washington, Seattle, USA). http://hdl.handle.net/1773/45398

Khan, A., Mosegaard, K., & Rasmussen, K. L. (2000). A new seismic velocity model for the Moon from a Monte Carlo inversion of the Apollo lunar seismic data. *Geophysical Research Letters, 27*(11), 1591–1594. https://doi.org/10.1029/1999GL008452

Kindler, P., Guillevic, M., Baumgartner, M. F., Schwander, J., Landais, A., & Leuenberger, M. (2014). Temperature reconstruction from 10 to 120 kyr b2k from the NGRIP ice core. *Climate of the Past, 10*(2), 887–902. https://doi.org/10.5194/cp-10-887-2014

Koutnik, M. R., Fudge, T. J., Conway, H., Waddington, E. D., Neumann, T. A., Cuffey, K. M., Taylor, K. C., et al. (2016). Holocene accumulation and ice flow near the West Antarctic Ice Sheet Divide ice core site. *Journal of Geophysical Research: Earth Surface, 121*(5), 907–924. https://doi.org/10.1002/2015JF003668

Lamb, K. D., Clouser, B. W., Bolot, M., Sarkozy, L., Ebert, V., Saathoff, H., Mohler, O., & Moyer, E. J. (2017). Laboratory measurements of HDO/$H_2O$ isotopic fractionation during ice deposition in simulated cirrus clouds. *Proceedings of the National Academy of Sciences, 114*(22), 5612–5617. https://doi.org/10.1073/pnas.1618374114

Landais, A., Barnola, J.M., Kawamura, K., Caillon, N., Delmotte, M., van Ommen, T., Dreyfus, G., Jouzel, J., Masson-Deltmotte, V., Minster, B., Freitag, J., Leuenberger, M., Schwander, J., Huber, C., Etheridge, D., & Morgan, V. (2006). Firn-air $\delta^{15}$N in modern polar sites and glacial-interglacial ice: a model-data mismatch during glacial periods in Antarctica? *Quaternary Science Reviews, 25*(1-2), 499–62. https://doi.org/10.1016/j.quascirev.2005.06.007

Lazzara, M. A., Keller, L. M., Markle, T., & Gallagher, J. (2012). Fifty-year Amundsen–Scott South Pole station surface climatology. *Atmospheric Research*, 118, 240–259. https://doi.org/10.1016/j.atmosres.2012.06.027

Lee, J.-E., Fung, I., DePaolo, D. J., & Otto-Bliesner, B. (2008). Water isotopes during the Last Glacial Maximum: New general circulation model calculations. *Journal of Geophysical Research, 113*(D19). https://doi.org/10.1029/2008JD009859

Li, J., & Zwally, H. J. (2015). Response times of ice-sheet surface heights to changes in the rate of Antarctic firn compaction caused by accumulation and temperature variations. *Journal of Glaciology, 61*(230), 1037–1047. https://doi.org/10.3189/2015JoG14J182

Ligtenberg, S. R. M., Helsen, M. M., & Van den Broeke, M. R. (2011). An improved semi-empirical model for the densification of Antarctic firn. *The Cryosphere, 5*, 809–819. https://doi.org/10.5194/tc-5-809-2011

Lilien, D. A., Fudge, T. J., Koutnik, M. R., Conway, H., Osterberg, E. C., Ferris, D. G., Stevens, C. M., et al. (2018). Holocene Ice-Flow Speedup in the Vicinity of the South Pole. *Geophysical Research Letters, 45*(13), 6557–6565. https://doi.org/10.1029/2018GL078253

Looyenga, H. (1965). Dielectric constants of heterogeneous mixtures. *Physica, 31*(3), 401–406. https://doi.org/10.1016/0031-8914(65)90045-5

Lorius, C., Jouzel, J., Raynaud, D., Hansen, J., & Le Treut, H. (1990). The ice-core record: climate sensitivity and future greenhouse warming. *Nature, 347*(6289), 139–145. https://doi.org/10.1038/347139a0

Lundin, J. M., Stevens, C. M., Arthern, R., Buizert, C., Orsi, A., Ligtenberg, S. R., Harris, P., et al. (2017). Firn Model Intercomparison Experiment (FirnMICE). *Journal of Glaciology, 63*(239), 401–422. https://doi.org/10.1017/jog.2016.114

Luz, B., & Barkan, E. (2010). Variations of $^{17}$O/$^{16}$O and $^{18}$O/$^{16}$O in meteoric waters. *Geochimica et Cosmochimica Acta, 74*(22), 6276–6286. https://doi.org/10.1016/j.gca.2010.08.016

MacAyeal, D. R. (1993). Binge/purge oscillations of the Laurentide ice sheet as a cause of the North Atlantic's Heinrich events. *Paleoceanography, 8*(6), 775–784. https://doi.org/10.1029/93PA02200

Majoube, B. (1970). Fractionation factor of $^{18}$O between water vapour and ice. *Nature, 226*, 1242. https://doi.org/10.1038/2261242a0

Markle, B. R. (2017). *Climate dynamics revealed in ice cores: advances in techniques, theory, and interpretation* (Thesis (PH. D.) – University of Washington, 208 pp.). http://hdl.handle.net/1773/40391

Martinerie, P., Lipenkov, V. Y., Raynaud, D., Chappellaz, J., Barkov, N. I., % Lorius, C. (1994). Air content paleo record in the Vostok ice core (Antarctica): A mixed record of climatic and glaciological parameters. *Journal of Geophysical Research, 99*(D5), 10565. https://doi.org/10.1029/93JD03223

Masson-Delmotte, V., Jouzel, J., Landais, A., Stievenard, M., Johnsen, S.J., White, J. W. C., Werner, M., Sveinbjornsdottir, A. and Fuhrer, K. (2005). GRIP deuterium excess reveals rapid and orbital-scale changes in Greenland moisture origin. *Science, 309*, 118–121. https://doi.org/10.1126/science.1108575

Masson-Delmotte, V., Kageyama, M., Braconnot, P., Charbit, S., Krinner, G., Ritz, C., Gladstone, R. M., et al. (2006). Past and future polar amplification of climate change: climate model intercomparisons and ice-core constraints. *Climate Dynamics, 26*(5), 513–529. https://doi.org/10.1007/s00382-005-0081-9

Masson-Delmotte, V., Hou, S., Ekaykin, A., Jouzel, J., Aristarain, A., Bernardo, R. T., Frezzotti, M., et al. (2008). A review of Antarctic surface snow isotopic composition: Observations, atmospheric circulation, and isotopic modeling. *Journal of Climate, 21*(13), 3359–3387. https://doi.org/10.1175/2007JCLI2139.1

Metropolis, N., Rosenbluth, A. W., Rosenbluth, M. N., Teller, A. H., & Teller, E. (1953). Equation of state calculations by fast computing machines. *The Journal of Chemical Physics, 21*(6), 1087–1092. https://doi.org/10.1063/1.1699114

Monnin, E., Steig, E. J., Siegenthaler. U., Kawamura, K., Schwander, J., Stauffer, B., Morse, D. L., Stocker, T. F., Barnola, J. M., Bellier, B., Raynaud, D., & Fischer, H. (2004). Evidence for substantial accumulation rate variability in Antarctica during the Holocene through synchronization of $CO_2$ in the Taylor Dome, Dome C and DML ice cores. *Earth and Planetary Science Letters, 224*, 45–54. https://doi.org/10.1016/j.epsl.2004.05.007

Mosegaard, K., & Tarantola, A. (1995). Monte Carlo sampling of solutions to inverse problems. *Journal of Geophysical Research: Solid Earth, 100*(B7), 12431–12447. https://doi.org/10.1029/94JB03097

Mosegaard, K. (1998). Resolution analysis of general inverse problems through inverse Monte Carlo sampling. *Inverse Problems, 14*(3), 405. https://doi.org/10.1088/0266-5611/14/3/004

Mosegaard, K., & Tarantola, A. (2002). Probabilistic approach to inverse problems. In W. Lee, P. Jennings, C. Kisslinger, & H. Kanamori (Eds.), *International Handbook of Earthquake & Engineering Seismology (Part A)* (237–265). Academic Press.

Mosegaard, K., & Sambridge, M. (2002). Monte Carlo analysis of inverse problems. *Inverse problems, 18*(3), R29. https://doi.org/10.1088/0266-5611/18/3/201

Neumann, T. A., Conway, H., Price, S., Waddington, E. D., & Morse, D. L. (2008). Holocene accumulation and ice-sheet dynamics in central West Antarctica. *Journal of Geophysical Research, 113*, (F2). https://doi.org/10.1029/2007JF000764

Nye, J. (1963). Correction factor for accumulation measured by the thickness of the annual layers in an ice sheet. *Journal of Glaciology, 4*(36), 785–788. https://doi.org/10.3189/S0022143000028367

Parrenin, F., Remy, F., Ritz, C., Siegert, M. J., & Jouzel, J. (2004). New modeling of the Vostok ice flow line and implication of the glaciological chronology of the Vostok ice core. *Journal of Geophysical Research, 109*, (D20). https://doi.org/10.1029/2004JD004561

Parrenin, F., Barker, S., Blunier, T., Chappellaz, J., Jouzel, J., Landais, A., Veres, D., et al. (2012). On the gas-ice depth difference (Δdepth) along the EPICA Dome C ice core. *Climate of the Past, 8*(2), 1089–1131. https://doi.org/10.5194/cpd-8-1089-2012

Parrenin, F., Masson-Delmotte, V., Kohler, P., Raynaud, D., Paillard, D., Schwander, J., Jouzel, J., et al. (2013). Synchronous change of atmospheric CO2 and Antarctic temperature during the last deglacial warming. *Science, 339*(6123), 1060–1063. https://doi.org/10.1126/science.1226368

Peltier, W.R. (2004). Global glacial isostasy and the surface of the ice-age Earth: The ICE-5G (VM2) Model and GRACE. *Ann. Rev. Earth and Planet. Sci., 32*, 111–149. https://doi.org/10.1146/annurev.earth.32.082503.144359

Pollard, D., & DeConto, R. M. (2009). Modelling West Antarctic ice sheet growth and collapse through the past five million years. *Nature, 458*(7236), 329–332. https://doi.org/10.1038/nature07809

Price, P. B., Nagornov, O. V., Bay, R., Chirkin, D., He, Y., Miocinovic, P., Richards, A., Woschnagg, K., Koci, B., & Zagorodnov, V., (2002). Temperature profile for glacial ice at the South Pole: implications for life in a nearby subglacial Lake. *Proceedings of the National Academy of Sciences, 99*(12), 7844–7847. https://doi.org/10.1073/pnas.082238999

Raymond, C. (1983). Deformation in the vicinity of ice divides. *Journal of Glaciology, 29*(103), 357—373. https://doi.org/10.3189/S0022143000030288

Roy, K., & Peltier, W. R. (2015). Glacial isostatic adjustment, relative sea level history and mantle viscosity: reconciling relative sea level model predictions for the US East coast with geological constraints. *Geophysical Journal International, 201*(2), 1156–1181. https://doi.org/10.1093/gji/ggv066.

Schoenemann, S. W., Steig, E. J., Ding, Q., Markle, B. R., & Schauer, A. J. (2014). Triple water-isotopologue record from WAIS Divide, Antarctica: Controls on glacial-interglacial changes in $^{17}O_{excess}$ of precipitation. *Journal of Geophysical Research: Atmospheres, 119*(14), 8741–8763. https://doi.org/10.1002/2014JD021770

Schwander, J., & Stauffer, B. (1984). Age difference between polar ice and the air trapped in its bubbles. *Nature, 311*(5981), 45–47. https://doi.org/10.1038/311045a0

Schwander, J., Stauffer, B., & Sigg, A. (1988). Air mixing in firn and the age of the air at pore close-off. *Annals of Glaciology, 10*, 141–145. https://doi.org/10.3189/S0260305500004328

Schwander, J. The transformation of snow to ice and the occlusion of gases, in: H. Oeschger, C.C. Langway Jr. (Eds.), The Environmental Record in Glaciers and Ice Sheets, John Wiley, New York, 1989, pp. 53–67.

Severinghaus, J. P., Sowers, T., Brook, E. J., Alley, R. B., & Bender, M. L. (1998). Timing of abrupt climate change at the end of the Younger Dryas interval from thermally fractionated gases in polar ice. *Nature, 391*(6663), 141–146. https://doi.org/10.1038/34346

Severinghaus, J. P., Grachev, A., & Battle, M. (2001). Thermal fractionation of air in polar firn by seasonal temperature gradients. *Geochemistry, Geophysics, Geosystems, 2*(7). https://doi.org/10.1029/2000GC000146

Severinghaus, J. (2019) "South Pole (SPICECORE) $^{15}N$, $^{18}O$, $O_2/N_2$ and Ar/N)2" U.S. Antarctic Program (USAP) Data Center. https://doi.org/10.15784/601152.

Sigl, M., Fudge, T. J., Winstrup, M., Cole-Dai, J., Ferris, D., McConnell, J. R., Bisiaux, M., et al. (2016). The WAIS Divide deep ice core WD2014 chronology–Part 2: Annual-layer counting (0–31 ka BP). *Climate of the Past, 12*(3), 769–786. https://doi.org/10.5194/cp-12-769-2016

Sime, L. C., Hopcroft, P. O., & Rhodes, R. H. (2019). Impact of abrupt sea ice loss on Greenland water isotopes during the last glacial period. *Proceedings of the National Academy of Sciences, 116*(10), 4099–4104. https://doi.org/10.1073/pnas.1807261116

Simonsen, S. B., Johnsen, S. J., Popp, T. J., Vinther, B. M., Gkinis, V., & Steen-Larsen, H. C. (2011). Past surface temperatures at the NorthGRIP drill site from the difference in firn diffusion of water isotopes. *Climate of the Past, 7*(4), 1327–1335. https://doi.org/10.5194/cp-7-1327-2011

Simonsen, S. B., Stenseng, L., Ađalgeirsdóttir, G., Fausto, R. S., Hvidberg, C. S., & Lucas-Picher, P. (2013). Assessing a multilayered dynamic firn-compaction model for Greenland with ASIRAS radar measurements. *Journal of Glaciology, 59*(215), 545–558. https://doi.org/10.3189/2013JoG12J158

Sowers, T., Bender, M., Raynaud, D., & Korotkevich, Y. S. (1992). $\delta^{15}N$ of $N_2$ in air trapped in polar ice: A tracer of gas transport in the firn and a possible constraint on ice age-gas age differences. *Journal of Geophysical Research: Atmospheres, 97*(D14), 15683–15697. https://doi.org/10.1029/92JD01297

Steen-Larsen, H. C., Waddington, E. D., & Koutnik, M. R. (2010). Formulating an inverse problem to infer the accumulation-rate pattern from deep internal layering in an ice sheet using a Monte Carlo approach. *Journal of Glaciology, 56*(196), 318–332. https://doi.org/10.3189/002214310791968476

Steig, E. J., Grootes, P. M., & Stuiver, M. (1994). Seasonal precipitation timing and ice core records. *Science, 266*, 1885–1886. https://doi.org/10.1126/science.266.5192.1885

Steig, E. J., Ding, Q., White, J. W. C., Küttel, M., Rupper, S. B., Neumann, T. A., Neff, P. D., Gallant, A. J. E., Mayewski, P. A., Taylor, K. C., Hoffmann, G., Dixon, D. A., Schoenemann, S., Markle B. M., Schneider, D. P., Fudge, T. J., Schauer, A. J., Teel, R. P., Vaughn, B., Burgener, L., Williams, J., & Korotkikh, E. (2013). Recent climate and ice-sheet change in West Antarctica compared to the past 2000 years. *Nature Geoscience, 6*(5), 372. https://doi.org/10.1038/ngeo1778

Steig, E. J., Gkinis, V., Schauer, A. J., Schoenemann, S. W., Samek, K., Hoffnagle, J., Tan, S. M., et al. (2014). Calibrated high-precision $^{17}$O-excess measurements using cavity ring-down spectroscopy with laser-current-tuned cavity resonance. *Atmospheric Measurement Techniques, 7*, 2421–2435. https://doi.org/10.5194/amt-7-2421-2014

Steig, E. J., T. R. Jones, A. J. Schauer, E. C. Kahle, V. A. Morris, B. H. Vaughan, L. Davidge, & White, J. W. C. (2021). Continuous-flow analysis of $\delta^{17}$O, $\delta^{18}$O, and $\delta$D of $H_2O$ on an ice core from the South Pole. *Frontiers in Earth Science, 9*, 640292. https://doi.org/10.3389/feart.2021.640292

Stevens, C. M., Verjans, V., Lundin, J., Kahle, E. C., Horlings, A. N., Horlings, B. I., & Waddington, E. D. (2020). The Community Firn Model (CFM) v1. 0. *Geoscientific Model Development, 13*(9), 4355–4377. https://doi.org/10.5194/gmd-13-4355-2020

Tarantola, A. (1987). Inverse problem theory: Methods for data fitting and model parameter estimation. *Elsevier Science*, Amsterdam.

van der Wel, G., Fischer, H., Oerter, H., Meyer, H., & Meijer, H. A. J. (2015). Estimation and calibration of the water isotope differential diffusion length in ice core records. *The Cryosphere, 9*(4), 1601–1616. https://doi.org/10.5194/tc-9-1601-2015

Veres, D., Bazin, L., Landais, A., Toyé Mahamadou Kele, H., Lemieux-Dudon, B., Parrenin, F., Chappellaz, J., et al. (2013). The Antarctic ice core chronology (AICC2012): an optimized multi-parameter and multi-site dating approach for the last 120 thousand years. *Climate of the Past, 9*(4), 1733–1748. https://doi.org/10.5194/cp-9-1733-2013

WAIS Divide Project Members (2013). Onset of deglacial warming in West Antarctica driven by local orbital forcing. *Nature, 500*(7463), 440–444. https://doi.org/10.1038/nature12376

Werner, M., Mikolajewicz, U., Heimann, M., & Hoffmann, G. (2000). Borehole versus isotope temperatures on Greenland: Seasonality does matter. *Geophysical Research Letters, 27*(5), 723–726. https://doi.org/10.1029/1999GL006075

Werner, M., Jouzel, J., Masson-Delmotte, V., & Lohmann, G. (2018). Reconciling glacial Antarctic water stable isotopes with ice sheet topography and the isotopic paleothermometer. *Nature Communications, 9*(1), 1-10. https://doi.org/10.1038/s41467-018-05430-y

Whillans, I. M., & Grootes P. M. (1985). Isotopic diffusion in cold snow and firn. *Journal of Geophysical Research, 90*(D2), 3910–3918. https://doi.org/10.1029/JD090iD02p03910

Whitehouse, P. L., Bentley, M. J., & Le Brocq, A. M. (2012). A deglacial model for Antarctica: geological constraints and glaciological modelling as a basis for a new model of Antarctic glacial isostatic adjustment. *Quaternary Science Reviews, 32*, 1–24. https://doi.org/10.1016/j.quascirev.2011.11.016

Winski, D. A., Fudge, T. J., Ferris, D. G., Osterberg, E. C., Fegyveresi, J. M., Cole-Dai, J., Buizert, C., Epifanio, J., Brook, E. J., Beaudette, R., Severinghaus, J., Sowers, T., Steig, E. J., Kahle, E. C., Jones, T. R., Morris, V., Aydin, M., Nicewonger, M. R., Casey, K. A., Alley, R. B., Waddington, E. D., & Iverson, N.

A. (2019). The SP19 chronology for the South Pole Ice Core–Part 1: volcanic matching and annual layer counting. *Climate of the Past, 15*(5), 1793–1808. https://doi.org/10.5194/cp-15-1793-2019

York, D., Evensen, N. M., Martınez, M. L., & De Basabe Delgado, J. (2004). Unified equations for the slope, intercept, and standard errors of the best straight line. *American Journal of Physics, 72*(3), 367–375. https://doi.org/10.1119/1.1632486